The Hong Kong Polytechnic University
Department of Electrical Engineering

OPTICAL PERFORMANCE MONITORING FOR NEXT GENERATION COHERENT OPTICAL COMMUNICATION SYSTEMS

Shen Shunrong

A thesis submitted in partial fulfillment of the requirements

for the degree of Master of Philosophy

May 2011

CERTIFICATION OF ORIGINALITY

I hereby declare that this thesis is my own work and that, to the best of my knowledge and belief, it reproduces no material previously published or written, nor material that has been accepted for the award of any other degree or diploma, except where due acknowledgement has been made in the test.

(Signed)

Shen Shunrong (Name of student)

ABSTRACT

Optical performance monitoring (OPM) is a technique used to assess the performance and limiting factors of optical networks, especially the physical channel impairments. In conventional intensity modulation/direct detection (IM/DD) systems, only linear channel impairments including optical signal-to-noise ratio (OSNR), chromatic dispersion (CD) and polarization mode dispersion (PMD) are concerned by network management. The monitoring data from OPM enables the network management system to implement impairment-aware route-wavelength-assignment (IA-RWA) algorithms for better quality of transmission (QoT) by taking into account real-time signal distortions in various links between the source and destination during route-wavelength assignment. Moreover, physical states of a particular channel provided by OPM can help automatic negotiation of optimal configuration of network components between two transmission ends to achieve more flexible, scalable reliable and efficient network operation. Fault localization using conventional fault diagnose techniques is limited to identifying serious signal degradation and complete connection lost. Since OPM directly provide the state of the physical channel, it can not only identify subtle faults such as drift in operating parameters of system components but can also differentiate the origin/cause of the faults. It is believed that OPM will be a fundamental function instead of a subroutine in future optical communication networks.

Coherent detection with electronic digital signal processing (DSP) receivers is considered as the most promising solution for the next generation optical networks

transmitting at 100 Gbps and beyond. Besides the merits of OPM discussed above, information of critical channel parameters monitored by OPM is necessary for improving the performance of channel equalization function such as backpropagation (BP) at the coherent receiver. However, high order modulation formats used in coherent communication systems such as QPSK and 16 QAM also bring new challenges to OPM. In addition to the aforementioned linear channel impairments, nonlinear impairments and other sources of phase noise, including self-phase modulation (SPM), cross phase modulation (XPM), laser phase noise and laser frequency offset between the transmitter and receiver can no longer be simply ignored. High quality of service (QoS) in the next generation coherent networks, therefore, will rely on OPM to provide accurate information of these impairments for system configuration, packet switching and channel impairment compensation. As the control plane of the management system requires a complete map of real-time channel conditions across various links in a network to coordinate routing for maximum network efficiency, OPM is desired to be deployed at intermediate network nodes such as optical cross-connect (OXC) unit as well as end terminals. Thus, the cost of OPM becomes another major concern. Moreover, modern OPM is also expected to be transparent to various modulation formats and bit rates that may coexist in coherent optical systems.

In this thesis, we first studied the application of asynchronous amplitude histogram (AAH) in OSNR monitoring for higher order modulation formats. Since no timing/clock recovery circuitries are required and the sampling speed could be

much lower than the symbol rate, AAH can significantly reduce the cost of monitoring units. Simulation results indicate that the proposed technique can be applied to *M* order quadrature amplitude modulation (QAM) formats with high accuracy. The influences of CD and PMD are also evaluated. As independent and simultaneous monitoring of OSNR, CD and PMD are almost impossible using AAH alone, we further proposed the use of artificial neural network (ANN) trained with AAH for simultaneous monitoring of multiple channel impairments. Simulation results verified that the combination of ANN and AAH can independently monitor OSNR, CD and PMD simultaneously with high accuracy with a wide monitoring range.

For monitoring of nonlinear parameters of the channel, we proposed a DSP-based monitoring technique using the statistics of the received pilot symbols. It is demonstrated that the proposed nonlinear parameter monitoring technique can simultaneously monitor phase noise introduced by laser linewidth, laser frequency offset between the transmitter and local oscillator and ASE noise. The number of spans between the two transmission ends can be obtained as well in case such information is not available from upper level network protocols. Finally, faults can also be localized by evaluating the relation between the variance of received signal power and phase.

PUBLICATIONS ARISING FROM THE THESIS

1. T. S. R. Shen, K. Meng, A. P. T. Lau and Z. Y. Dong, "Optical Performance Monitoring Using Artificial Neural Network Trained with Asynchronous Amplitude Histograms", *IEEE Photonics Technology Letters*, vol. 22, no. 22, pp. 1665-1667, Nov. 2010.
2. T. S. R. Shen, A. P. T. Lau and G. N. Liu, "OSNR Monitoring for Higher Order Modulation Formats Using Asynchronous Amplitude Histogram", *IEEE Photonics Technology Letters*, vol. 22, no. 22, pp. 1632-1634, Nov. 2010.
3. T. S. R. Shen, A. P. T. Lau and C. Yu, "Simultaneous and Independent Multi-Parameter Monitoring and Fault Localization for DSP-based Coherent Communication Systems", Optics Express, vol. 18, no. 23, pp. 23608-23619, Oct. 2010.
4. T. S. R. Shen, A. P. T. Lau and C. Yu, "Joint Nonlinear Parameters and OSNR Monitoring for DSP-based Coherent Systems", in The 15th Optoelectronics and Communications Conference (OECC), Sapporo, Japan, 2010
5. A.P.T. Lau, Q. Sui, T.S.R. Shen, F.N. Khan and C. Lu, " Optical Performance Monitoring Using Statistical Signal Processing," International Conference on Advanced Infocomm. Technology (ICAIT), Haikou, Hainan Island, China, Jul. 2010.
6. A.P.T. Lau, Q. Sui, T.S.R. Shen, F.N. Khan and C. Lu, " Optical Performance Monitoring Using Statistical Signal Processing," International Conference on Optical Communications Networks (ICOCN), Nanjing, China, Oct. 2010.

ACKNOWLEDGMENT

I would like to thank my parents who always stand by my side and help me through the darkest days.

I would also like to express my sincere gratitude to my supervisor Dr. Alan Lau for giving me the opportunity to work with him and other talents in the Photonics Research Center of The Hong Kong Polytechnic University. His professional and patient guidance is the key to my achievements and will have profound influence on my future career.

Finally, I would like to thank Prof. Tam, Prof. Lu and all other people who have shared their wisdoms and kindness during my study. Without your generous help, I will not be the one who I am. Thank you.

TABLE OF CONTENTS

Abstract i

Publications arising from the thesis vi

Acknowledgment vii

Table of Contents viii

Abbreviations xi

Table of Figures xiii

Chapter 1 Introduction 1

1.1 The need for OPM 3

1.2 Challenges in OPM 5

1.3 OPM in coherent optical communication systems 7

1.4 Organization of the thesis 8

Chapter 2 Literature Review 10

2.1 OPM using RF spectrum analysis 10

2.2 OPM using asynchronous amplitude histogram 17

2.3 OPM using artificial neural network 26

2.3.1 Artificial neural network 26

2.3.2 Review of OPM using ANN 28

2.3.3 Other OPM techniques based on machine learning algorithm 33

2.4 OPM for coherent communication systems 35

2.4.1 Coherent optical communications..... 35

2.4.2 Frequency offset estimation for optical coherent receiver..... 37

2.4.3 Laser linewidth monitoring in coherent optical communication systems 47

2.4.4 Estimation of fiber Kerr nonlinearity..... 50

Chapter 3 OSNR Monitoring for Higher Order Modulation Formats Using Asynchronous Amplitude Histogram 54

3.1 Operating Principles..... 54

3.2 Simulation results and discussions. 58

3.3 Summary 61

Chapter 4 Optical Performance Monitoring Using Artificial Neural Network Trained with Asynchronous Amplitude Histograms 62

4.1 Principles of ANN using AAH..... 63

4.1.1 RBF neural network..... 63

4.1.2 Asynchronous Amplitude Histogram 64

4.2 Simulations Results and discussions..... 66

4.2.1 RZ-DQPSK Systems..... 66

4.2.2 NRZ-16-QAM Systems 68

4.3 Summary 70

Chapter 5 Simultaneous and Independent Multi-Parameter Monitoring and Fault Localization for DSP-based Coherent Communication Systems 72

5.1 Operating Principles 74

5.1.1 System model 74

5.1.2 Simultaneous and independent multi-parameter monitoring 79

5.2 Simulation Results and Discussions 82

5.3 Receiver-based fault localization using statistics of received pilot symbols 86

5.4 Summary 88

Chapter 6 Summary and Future Work 90

6.1 Summary of the work 90

6.2 Suggestion for future work 93

References 95

ABBREVIATIONS

AAH	Asynchronous amplitude histogram
ANN	Artificial neural network
ASE	Amplified spontaneous emission
BER	Bit error rate
BP	Backpropagation
CD	Chromatic dispersion
DCF	Dispersion compensation fiber
DI	Delay interferometer
DSP	Digital signal processing
ER	Extinction Ratio
FWM	Four-wave mixing
IM/DD	Intensity modulation/Direct detection
IA-RWA	Impairment-aware route wavelength assignment
OPM	Optical performance monitoring
OSNR	Optical signal-to-noise ratio
PSP	Principal State of Polarization
OXC	Optical cross connect

QAM	Quadrature amplitude modulation
QoS	Quality of service
QoT	Quality of transmission
RBF	Radial basis function
RF	Radio frequency
SMF	Single-mode fiber
SPM	Self-phase modulation
XPM	Cross-phase modulation

TABLE OF FIGURES

Fig. 2.1 Basic principle of using RF fading for online CD monitoring. 11

Fig. 2.2 Dependency of RF spectra of an 8 GHz subcarrier tone on different amount of accumulated CD in a 10 Gbps transmission system. 12

Fig. 2.3 RF tone power as a function of accumulated CD for different subcarrier frequencies. 12

Fig. 2.4 BER against received optical powers for different experimental setups [17]. ... 13

Fig. 2.5 PSD of 10 Gbps (a) NRZ-DPSK (b) RZ-DPSK system with different accumulated dispersion values. 14

Fig. 2.6 $F(\beta_2 L)/F(0)$ as a function of accumulated CD. 15

Fig. 2.7 Theoretical, experimental and simulation results of CD monitoring for (a) NRZ-DPSK and (b) RZ-DPSK systems. 15

Fig. 2.8 Dependency of CD monitoring using RF spectrum on (a) OSNR (b) PMD (c) nonlinearity. 17

Fig. 2.9 Comparisons between histograms and corresponding eye diagrams for different OSNR. 19

Fig. 2.10 Comparison of histograms for different OSNR changed by varying signal power. 19

Fig. 2.11 Calibration graph of evaluated Q_{avg} against actual *Q* factor for different α 20

Fig. 2.12 Dependence of asynchronous amplitude histogram on CD for 10 Gbps NRZ systems (a) Ps = -35 dBm, CD = 0 ps/nm and (b) Ps = -35 dBm, CD = 680 ps/nm. 21

Fig. 2.13 Definition of $X_{\sigma 1}$ and X_{μ}. 22

Fig. 2.14 Dependence of $X_{\sigma 1} + X_{\mu}$ on (a) CD and (b) OSNR for 10 Gbps NRZ systems when α =0.2, 0.3 and 0.4. 22

Fig. 2.15 Waveform of RZ-DPSK pulse pair with (a) π phase difference and (b) 0 phase difference. 23

Fig. 2.16 Pulse pair intensity at point B, A1 and A2 for different CD. 24

Fig. 2.17 Asynchronous amplitude histogram of RZ-DPSK signal. 25

Fig. 2.18 Experimental and simulation results of (a) estimated DF versus CD. (b) estimated AQ versus OSNR (c) estimated AQ as a function of CD for different OSNR in RZ-DPSK system. 25

Fig. 2.19 Experimental and simulation results for PMD monitoring in RZ-DPSK system under 250 ps/nm chromatic dispersion. 26

Fig. 2.20 Structure of a typical artificial neural network. 27

Fig. 2.21 Eye diagrams of 10Gbps NRZ-OOK system with OSNR = 32 dB and various channel impairments (a) No impairment (b) DGD only (C) CD only and (d) DGD and CD. 29

Fig. 2.22 (a) OSNR (b) CD and (c) DGD monitoring results for 10 Gbps RZ-DPSK channel..... 30

Fig. 2.23 Asynchronous constellation diagrams distorted by (a) None (b) DGD (c) CD and (d) DGD and CD. 32

Fig. 2.24 Partitioned asynchronous constellation diagram for feature extractions for OPM using ANN. 32

Fig. 2.25 (a) OSNR (b) CD and (c) DGD monitoring results in 40 Gbps RZ-DQPSK system. 33

Fig. 2.26 Comparison of eye diagram and phase portrait for NRZ signal (a) OSNR = 35 dB and no impairment (b) OSNR = 25 dB (c) OSNR = 35 dB, CD = 800 ps/nm and (d) OSNR = 35 dB, DGD = 40 ps. 34

Fig. 2.27 Simulation results of simultaneous monitoring of CD and DGD_{eff} for 40 Gbps NRZ-DPSK signals. 35

Fig. 2.28 Balanced detector for coherent receiver. 36

Fig. 2.29 Structure of a two-stage FOE. 38

Fig. 2.30 Phase error output of Gardner algorithm versus timing offsets for different frequency offsets. 39

Fig. 2.31 Normalized MPE versus frequency offset for different OSNR. 39

Fig. 2.32 Experimental setup of 42.8 Gbit/s PolMux RZ-QPSK system PMOC is the polarization-maintaining optical coupler. VOA is the variable optical

attenuator. EDFA is the erbium-doped fiber amplifier and PC is the polarization controller. 40

Fig. 2.33 BER performance of the experimental system using dual-stage cascaded FOE and FFT-based FOE for frequency offset at -1 GHz and 3 GHz. 41

Fig. 2.34 Comparison of operation window of proposed dual stage FOE and FFT-based FOE. 41

Fig. 2.35 Phase spectrum of the received QPSK signals with a frequency offset of 0.5 GHz..... 44

Fig. 2.36 $\langle \varphi_{d,n} \rangle$ and $\mathrm{Arg}[\exp(j2\pi\Delta f n T_s)]$ versus t for $\Delta f > 0$. 44

Fig. 2.37 Block diagram of proposed FOE (a) Estimator of frequency offset (b) Complete structure of FOE including estimation of the sign of frequency offset. 45

Fig. 2.38 Estimation error of frequency offset in the range of [-2.4 GHz, 2.4 GHz]. The SNR in electrical domain is 12 dB and 1000 independent trials are simulated for each frequency offset value. 46

Fig. 2.39 Mean estimation error versus SNR for different sample size. The frequency offset is 1 GHz and 5000 trials are simulated for each SNR. 47

Fig. 2.40 Frequency variance spectrum (a) with modulation and (b) without modulation on laser frequency 49

Fig. 2.41 Estimated linewidth versus true laser linewidth in the range of 100 kHz to 1 MHz. 50

Fig. 2.42 Experiment setup for nonlinear refractive index measurement using SPM. 51

Fig. 2.43 Experiment setup for fiber nonlinearity measurement using XPM-based technique..... 52

Fig. 3.1 Eye diagrams and corresponding asynchronous amplitude histograms for a 25 GSym/s NRZ-16-QAM system with (a) OSNR = 20 dB; (b) OSNR = 30 dB. 55

Fig. 3.2 Asynchronous amplitude histograms for 25 GSym/s NRZ-64-QAM signals with (a) OSNR = 20 dB; (b) OSNR = 30 dB..... 57

Fig. 3.3 Simulation setup for OSNR monitoring of 25 GSym/s NRZ/RZ 16/64-QAM signals. 58

Fig. 3.4 F_{OSNR} versus OSNR for a 25 GSym/s NRZ-16-QAM system with various levels of (a) CD and (b) PMD 59

Fig. 3.5 F_{OSNR} versus OSNR for a 25 GSym/s RZ-16-QAM system with various levels of (a) CD and (b) PMD. 59

Fig. 3.6 F_{OSNR} versus OSNR for a 25 GSym/s NRZ-64-QAM system with various levels of (a) CD and (b) PMD. 59

Fig. 3.7 F_{OSNR} versus OSNR for a 25 GSym/s RZ-64-QAM system with various levels of (a) CD and (b) PMD. 60

Fig. 4.1 Structure of a typical MIMO RBF neural network..... 63

Fig. 4.2 Asynchronous amplitude histograms obtained from 40 Gbps RZ-DQPSK signals distorted by selected combinations of transmission impairments: (a) OSNR = 30 dB, CD = 0 ps/nm, DGD = 0 ps; (b) OSNR = 24 dB, CD = 0 ps/nm, DGD = 0 ps; (c) OSNR = 30 dB, CD = 100 ps/nm, DGD = 0 ps; (d) OSNR = 30 dB, CD = 0 ps/nm, DGD = 10 ps. 65

Fig. 4.3 (a) OSNR (b) CD and (c) DGD monitoring results for a 40 Gbps RZ-DQPSK system using ANN with AAH as inputs..... 67

Fig. 4.4 Asynchronous amplitude histograms obtained from 40 Gbps NRZ-16-QAM signals distorted by selected combinations of transmission impairments (a) OSNR = 30 dB, CD = 0 ps/nm, DGD = 0 ps; (b) OSNR = 25 dB, CD = 0 ps/nm, DGD = 0 ps; (c) OSNR = 30 dB, CD = 250 ps/nm, DGD = 0 ps; (d) OSNR = 30 dB, CD = 0 ps/nm, DGD = 10 ps. 69

Fig. 4.5 (a) OSNR (b) CD and (c) PMD monitoring results for a 40 Gbps NRZ-16-QAM system using ANN with AAH as inputs. 70

Fig. 5.1 (a) In a dynamic optical network with ROADMs, signal may travel through different routes even for a given source and destination. This results in variations of the number of spans *N* as well as other parameters of the overall transmission link. (b) *Q*-factor vs. launch power for a NRZ-16-QAM system with length 1600 km and 10% CD under-compensation per span.

System performance is sensitive to the accuracies of the parameters used in BP. 73

Fig. 5.2 A coherent communication system setup with optical CD compensation 75

Fig. 5.3 A sequence of pilot symbols with alternating power levels P_1 and P_2 for the monitoring of laser linewidth, frequency offset, number of spans, fiber nonlinear parameters and OSNR of the link. The received signal is sampled at a rate of $1/T_s$ and the symbol rate $1/T$ is low enough such that the transmitted signal *E(t)* does not undergo any pulse shape distortion due to CD and/or PMD. 75

Fig. 5.4 (a) Estimated frequency offset vs. true frequency offset (b) Estimated laser linewidth vs. true laser linewidth for a 15-span system. Samples from 10^6 symbols are used for each estimate and the error bars indicate standard deviations of 10 independent estimates. 84

Fig. 5.5 (a) Estimated *N* vs. true *N*. (b) Estimated OSNR vs. true OSNR. (c) Estimated Λ_D vs. true Λ_D. Samples from 10^6 symbols are used for each estimate and the error bars indicate standard deviations of 10 independent estimates. The frequency offset and laser linewidth are 200 MHz and 100 kHz respectively. 86

Fig. 5.6 Change in variance of phase difference $\Delta\sigma^2_{\Delta\phi}(1)$ vs. fault location with $\Delta\sigma^2_{power}(P_k) = 6$, 8 and 10 dB for a 20-span link. Samples from 10^6 symbols are

used for each estimate and the error bars indicate standard deviations of 10 independent estimates. 88

Chapter 1
INTRODUCTION

Optical performance monitoring (OPM) is used to assess the performance of optical communication systems and monitor its limiting factors from the transmitted physical waveform. In general, OPM can be classified into two categories, including physical channel impairments monitoring which monitors critical channel parameters that have significant impact on signal quality on physical layer, and signal quality monitoring which evaluates bit-error rate (BER) and Q-factor of the received signals at the receiver [1]. As signal quality monitoring only measures overall signal distortion, network management system can only use it for simple logical judgment when two communication nodes are suddenly disconnected or signal quality at the receiver drops below a critical threshold. Furthermore, accurate signal quality monitoring such as BER estimation requires a relatively long period of time and hence may incur delay in system response to sudden performance degradation.

Physical channel impairments are currently the main research focus on performance monitoring for the next-generation optical communication systems. Typical channel impairments monitored by OPM in intensity modulation/direct detection (IM/DD) system are optical signal-to-noise ratio (OSNR), chromatic dispersion (CD) and polarization-mode dispersion (PMD). In particular, OSNR measures the ratio of signal power to in-band amplified spontaneous emission (ASE) noise introduced by optical amplifiers along the transmission link. Since OSNR

fundamentally dictates the overall transmission quality, OSNR monitoring provides a direct estimation of the signal quality at the receiver.

Chromatic dispersion is one of the major transmission impairments in high-speed optical communication systems. Because of the frequency-dependent nature of fiber refractive index, different frequency components of light travels at different speeds and a light pulse is broadened in the time-domain when propagating in the fiber. As the severity of CD increases with the square of bit rate and linearly with transmission distance, the maximum transmission rate and distance are limited. Although dispersion compensation fiber (DCF) is installed after each span of standard single mode fiber (SSMF) to eliminate the impairments induced by CD, it is difficult to compensate CD completely due to temperature, component aging and etc. In this case, the uncompensated CD will result in power penalty at the receiver.

Another linear impairment monitored in optical network is polarization-mode dispersion (PMD). The refractive index of the fiber could be polarization dependent ascribed to the fiber asymmetric geometry, impurity and environmental stress. As a result, the two orthogonal polarization components of a light pulse will propagate in the fiber at different speeds and the light pulse is broadened at the fiber output. This phenomenon is referred as polarization-mode dispersion (PMD). PMD effect varies randomly with time. It limits the ultimate channel capacity and is a major constraint of systems using polarization multiplexing.

1.1 The need for OPM

The rapid growth of internet-based service such as video streaming, e-commerce and online socialization drives the network traffic to increase exponentially in the past decade. Fueled by the huge demands, optical communication networks grow at an astonishing pace. After several generations of evolutions, modern optical networks have exceeded its predecessors by far much in terms of transmission capacity, number of connections and coverage area. Moreover, installation of reconfigurable optical add-drop multiplexers (ROADM) provides the optical networks with more flexibility to handle the dynamic traffic demands. Ascribed to its scale and complexity, however, management of optical network has also become more difficult and expensive. Insufficient knowledge of channel physical states always leads to installation of unnecessary network components and inefficient use of network resources [2].

Current packet switching and routing algorithms are mainly designed to reduce the hop number and probability of connection request blocking. However, effects of channel impairments of the selected links could be too large to be acceptable at the receiver. In such case, the network needs to calculate an alternative route for the packets and this process could take a long time and consume tremendous computation resources depending on the scale and complexity of the network. Impairment-aware route wavelength assignment (IA-RWA) is proposed for future optical networks to account for the channel impairments in the stage of routing calculation. However, to implement IA-RWA algorithms, the network control plane

requires the knowledge of the physical channel impairments. A connectivity verification stage is also suggested by both the IA-RWA algorithms and the GMPLS [3] to ensure the quality of transmission (QoT) before the data packets are routed. Therefore, OPM can provide real-time information for channel impairments and will be essential to future IA-RWA enabled networks. In addition to packet switching, OPM can potentially contribute to the realization of adaptive network topologies in optical communication networks. With access to instantaneous link parameters across the network, link management protocol is able to provide optimal reconfiguration of network resources to accommodate new transmission requests or terminate existing connections on demand.

Fault identification, localization and management in optical transport networks form another category of potential application of OPM. Different approaches have been so far proposed to localize the faults whenever alarms are triggered by network components [4-6]. However, these approaches usually assume complete loss of connection due to fiber cut, component failure and physical layer intrusion. Although Q-factor and BER monitoring at the receiving end can also detect serious system performance degradation, they are unable to identify the type of impairment that results in such degradations. Since OPM is designed to monitor various channel impairments at physical layer, the exact impairment that causes the communication failure or performance degradation can be identified. Also, by cross-referencing data from different monitoring units, the fault can be localized. With the information of both cause and location of the faults, fault isolation and restoration time can be

significantly shortened. On the other hand, the definition of channel fault in the next-generation optical networks is no longer constrained to complete channel disconnection, but should also accounts for subtle changes in channel impairments and drifts of component parameters related to nonlinearity, temperature fluctuation, component aging, channel crosstalk and other perturbations [7]. Although these "soft faults" will not interrupt the communication between two nodes instantly, knowing their occurrence, location and cause will be critical for maintaining high QoS of the network and prevent complete breakdown in the future [2]. Since these "soft faults" usually caused by changes in channel properties, only monitoring techniques having insight of the channel physical layer such as OPM is competent for the new monitoring task.

1.2 Challenges in OPM

One of the most challenging issues in OPM is the isolation of different types of channel impairments that may have similar impacts on the signal or could counteract with each other [8-10]. Linear impairments induced by both CD and PMD broaden the signal pulse in the time-domain, while the spectrum is broadened in presence of fiber nonlinearity. The interaction among channel impairments can easily make the monitoring results either overestimated or underestimated and it is difficult to identify unique signal distortion features for particular impairments. In addition to mixture of channel impairments, variation in pulse rise time, filter bandwidth, and other wavelength or polarization dependent channel parameters can all affect the accuracy of OPM.

OPM algorithms also need to balance the tradeoffs between monitoring range and accuracy. Current OPM techniques usually depend on variations in either the physical properties or the statistics of the signal to trace the corresponding impairments. Intuitively, if the monitored signal characteristic is highly sensitive to a particular impairment, the monitoring algorithm will be able to quantitatively measure the impairment even if its amount is considerably small. However, such signal characteristics will probably lose distinguishable features for monitoring quickly and therefore limit the range of monitoring. On the contrary, if the signal characteristic is relatively insensitive to the particular impairment, the performance monitoring technique can have a wider monitoring range.

Future optical network may accommodate different types of traffics. New technologies will be deployed to meet the rapid increasing traffic demand, while old systems will still be in-service for legacy problems. A mixture of various modulation formats and transmission rates are expected to coexist in the next-generation networks. Since it is impractical to build separate systems for monitoring of different data formats, modern OPM techniques should be transparent to modulation formats, bit rates and detection scheme that can be possibly used in future network.

Implementation cost of OPM is another major concern in OPM research. As it is desirable to have OPM functionalities at intermediate network nodes, the cost of installation and maintenance can quickly scale up with the size of the optical

network and hence OPM techniques that require expensive hardware are not preferable [11, 12].

1.3 OPM in coherent optical communication systems

Coherent detection is considered as one of the most promising technologies for the next-generation optical communication systems transmitting at 100 Gbps and beyond. By using high order modulation formats which modulate information on both signal amplitude and signal phase, coherent optical communication systems can achieve much higher spectral efficiency than conventional IM/DD systems. Advance in electronic technologies also ensures the implementation of digital signal processing algorithms for coherent optical communications.

However, the advanced coherent detection brings new challenges to OPM as well. Since signal phase is used to carry information, phase noise induced by fiber nonlinearity [13] and other sources of phase distortions such as laser phase noise and laser frequency offset can no longer be ignored, but should be part of OPM monitoring targets. In addition, the performance of DSP-based fiber nonlinearity compensation techniques proposed in recent years depend heavily on the accurate knowledge of channel parameters such as fiber nonlinear coefficient [14-16] and hence fiber nonlinearity monitoring in coherent optical systems is especially important. Moreover, different modulation formats transmitting at various bit rates are expected to coexist in future coherent optical networks [1, 2, 8]. Cost constraints will require future OPM techniques to be transparent to modulation formats and bit rates. Otherwise, deployment of multiple monitoring techniques and devices at one

location of the network will result in excessive expenditure and reduce the flexibility of future network expansion and upgrade.

In this thesis, three OPM techniques are proposed for monitoring of channel impairments in coherent optical systems. The first two techniques are based on asynchronous amplitude histogram (AAH) and artificial neural network (ANN) and focus on the monitoring of CD, PMD and especially OSNR. The proposed techniques' transparencies to modulation formats and bit rates are verified by simulations for QPSK, 16-QAM as well as 64-QAM formats with different bit rates. In addition, we also proposed the use of pilot symbols for simultaneous and independent monitoring of channel impairments that cause phase noise to coherently detected signals including fiber nonlinear parameter, laser phase noise and laser frequency offset.

1.4 Organization of the thesis

The rest of the thesis is divided into several chapters in the following manner:

Chapter 2 presents a literature review on OPM where several major classes of OPM techniques are described in more details.

Chapter 3 introduces an OSNR monitoring technique for higher-order modulation formats using asynchronous amplitude histogram. The AAHs of 16/64-QAM signals are thoroughly studied and a calibration factor from the AAH is defined for enhanced monitoring sensitivity and transparency to modulation format. The proposed technique is verified by simulations and its tolerance to CD and PMD is also evaluated.

In Chapter 4, the combination of AAH and ANN is studied for simultaneous monitoring of OSNR, CD and PMD. Superior monitoring range, accuracy and isolation of different impairments are demonstrated through simulations. To investigate the generality of the technique, simulations are conducted for both QPSK and 16-QAM systems.

In Chapter 5, we investigate the use of received power and phase of pilot sequence to jointly and independently monitor laser frequency offset, laser linewidth, fiber nonlinear coefficient, number of fiber spans and OSNR of a coherent system with a DSP-based receiver. Analytical expressions for the statistics of received pilot symbols are derived and corresponding analytical estimates of the monitoring parameters are provided. A transmission link with either full CD compensation or 10% CD under compensation is studied. In addition, it is shown that the changes in the statistics of received signal power and phase differences can be used for fault localization as well.

The last chapter summarizes the whole thesis by recapitulating the work presented in previous chapters. Potential improvements and future directions in OPM techniques are suggested.

Chapter 2
LITERATURE REVIEW

In the following sections, several classes of OPM techniques are discussed in details based on one or more related literatures.

2.1 OPM using RF spectrum analysis

Various channel impairments do not only distort signal in the time-domain, but also affect its spectrum. The way how signal spectrum is distorted by channel impairments depends on the type of impairment and the frequency range under concern. Hence, it is possible to distinguish and monitor channel impairments by analyzing the RF spectrum of the signal.

One common OPM technique using RF spectrum analysis is to transmit a subcarrier tone with the data signal and analyze its changes in power and phase at the receiver to estimate the overall channel impairments. In [17], a single in-band subcarrier tone is proposed for online chromatic dispersion monitoring and compensation. Fig. 2.1 illustrates the basic principle of the technique. The subcarrier tones in the upper and lower sidebands are in-phase at the transmitter. However, in presence of CD, a phase mismatch between the two components will accumulate during their propagation in the fiber. After O/E conversion at the receiver, the phase mismatch causes a power fading in the subcarrier tone as shown in Fig. 2.2. The detected photocurrent at the tone frequency fades as

$$I\left(f_{SC}\right) = I_0 m \cos\left(\frac{\pi f_{SC}^2 \lambda D L}{c}\right) \tag{2.1}$$

where I_0 is the peak photocurrent, m is the modulation depth, f_{SC} is the subcarrier tone frequency, λ is carrier wavelength, c is the speed of light in vacuum, D is the dispersion coefficient and L is the fiber length. By measuring the RF fading at the receiver and substituting it into Eq. 2.1, DL (the overall accumulated CD) can be estimated. It is also noted from Eq. 2.1 that the RF fading is periodic and there could be monitoring ambiguity if the accumulated dispersion exceeds one period of total fading. Since the period of RF fading is determined by tone frequency f_{SC}, it is important to select f_{SC} properly for optimal monitoring results. Fig. 2.3 compares the monitoring range of 7- and 9- GHz subcarrier tone in a 10 Gbps optical communication channel. As can be seen from the graph, the CD monitoring range is extended for 250 ps/nm by choosing 7 GHz instead of 9 GHz as the subcarrier frequency.

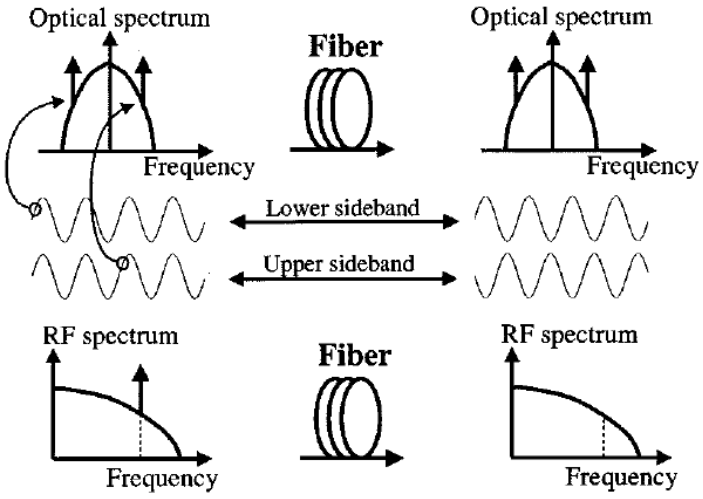

Fig. 2.1 Basic principle of using RF fading for online CD monitoring [17].

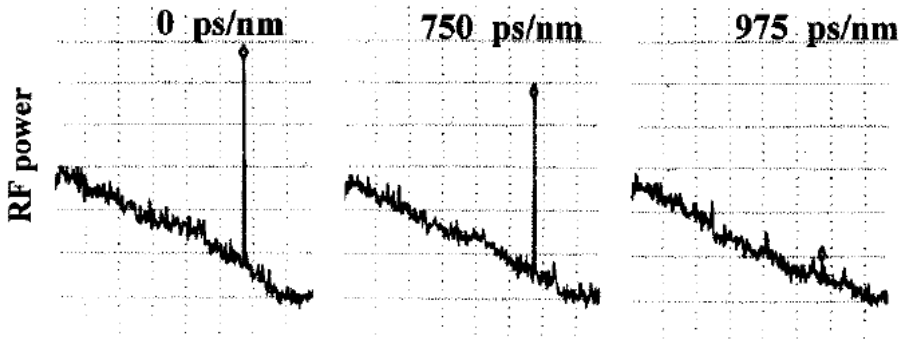

Fig. 2.2 Dependency of RF spectra of an 8 GHz subcarrier tone on different amount of accumulated CD in a 10 Gbps transmission system [17].

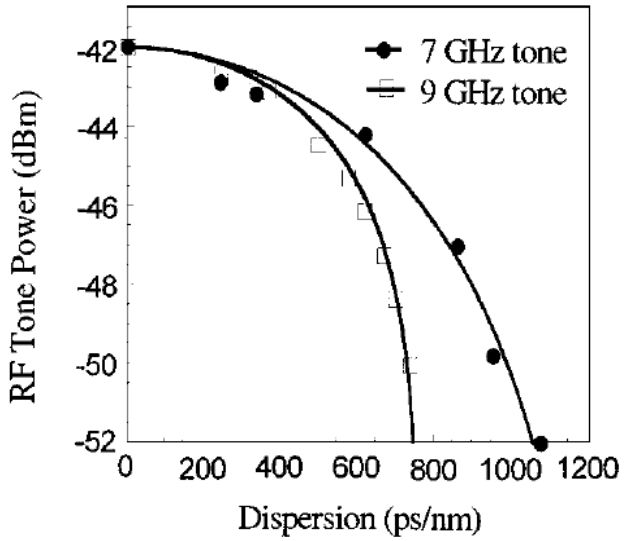

Fig. 2.3 RF tone power as a function of accumulated CD for different subcarrier frequencies [17].

To compensate for the effect of dispersion, Petersen *et al.* [17] use the measured tone power as a control signal to drive the nonlinearly chirped FBG with a dispersion range of -350 to -1000 ps/nm to compensate the accumulated CD of the link. The tone frequency is set to be 8.3 GHz and the accumulated dispersion after transmitting through 60 km fiber is 830 ps/nm. The BER measurements of the experimental setup are shown in Fig. 2.4. The dispersion compensation reduces the power penalty induced by CD from 2 dB to less than 0.5 dB which also demonstrate the capability of online CD monitoring using in-band subcarrier tone.

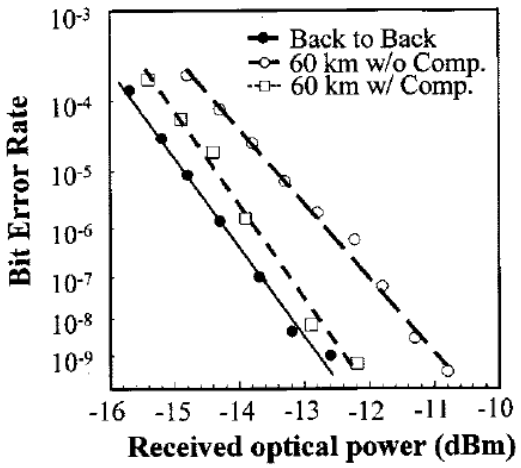

Fig. 2.4 BER against received optical powers for different experimental setups [17].

In addition to subcarrier tone, channel impairments may also be monitored by analyzing the whole RF spectrum. In [18], Zhao *et al.* demonstrated that the change in signal power within a frequency range is dependent on the amount of accumulated CD and such dependency can be used for wide-range CD monitoring in a wide range. Let $S_{yy}(f)$ be the power spectral density (PSD) of received signal, Fig. 2.5 shows the plot of $S_{yy}(f)$ in the range of 0 to 10 GHz for 10 Gbps NRZ- and RZ-DPSK systems with different accumulated dispersion values. As can be observed from the graphs, $S_{yy}(f)$ at higher frequencies increases with accumulated CD. This can be explained by the fact that CD redistributes the signal power from low frequency to high frequency. It is also noted that PSD of RZ-DPSK system increases more than NRZ-DPSK system for the same amount of CD. As RZ signal occupies a larger bandwidth than NRZ signal, CD induces more amplitude ripples on RZ signal than

NRZ signal which in turn causes more frequency components in high frequency domain and results in the discrepancy in PSD increment [18].

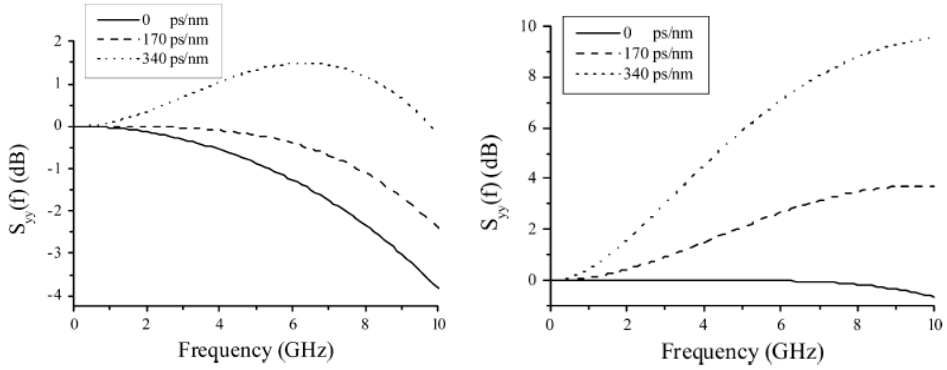

(a) (b)

Fig. 2.5 PSD of 10 Gbps (a) NRZ-DPSK (b) RZ-DPSK system with different accumulated dispersion values [18].

As the distribution of PSD of received signal is related to channel dispersion, Zhao *et al.* argues that accumulated CD may be monitored by measuring the change in total power within a frequency range, i.e. 0 to 10 GHz, which can be expressed by

$$F(\beta_2 L) = \int_0^{10G} S_{yy}(f)\,df \tag{2.2}$$

where β_2 is the second-order dispersion coefficient and L is the fiber length. The relative total power $F(\beta_2 L)/F(0)$ as a function of CD is plotted in Fig. 2.6. The sensitivity of power change varies with CD range which indicates a trade-off between monitoring sensitivity and range. Considering the balance among sensitivity, range and bit rate, 0 to 400 ps/nm is a reasonable range of residue CD for a 10 Gbps transmission system [18].

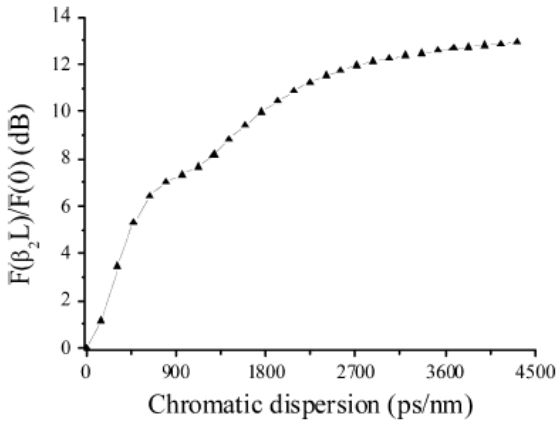

Fig. 2.6 $F(\beta_2 L)/F(0)$ as a function of accumulated CD [18].

Experimental and simulation results for CD monitoring for both NRZ- and RZ-DPSK system using the proposed technique are shown in Fig. 2.7. The relative RF power changes about 5.2 dB for CD from 0 to 400 ps/nm in NRZ-DPSK system and more than 15 dB in RZ-DPSK system for the same CD range. The monitoring sensitivity of RZ-DPSK is around 80 ps/nm/dBm which is more than twice as that of NRZ-DPSK.

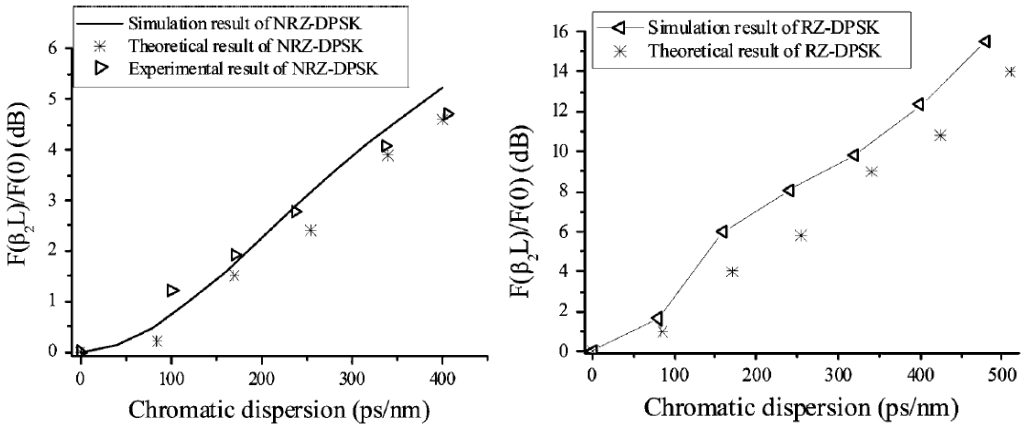

(a) (b)

Fig. 2.7 Theoretical, experimental and simulation results of CD monitoring for (a) NRZ-DPSK and (b) RZ-DPSK systems [18].

The effects of OSNR, first-order PMD and fiber nonlinearity on the monitoring results are also studied. As shown in Fig. 2.8(a), OSNR does not have significant impact on the monitoring, but only causes slight decrease in monitoring sensitivity and an approximate 5% degradation in monitoring accuracy when OSNR is reduced from 30 dB to 25 dB. DGD also does not modify the relative RF power curve by much as shown in Fig. 2.8(b). The monitoring errors are below 3% and 6% for DGD = 10 ps and 20 ps, respectively. Fig. 2.8(c) shows the simulated monitoring results for a 300-km long channel with different launch powers. The impact of SPM on CD monitoring is negligible until the signal power reaches 6 dBm when fiber nonlinearity becomes a dominant impairment in the channel.

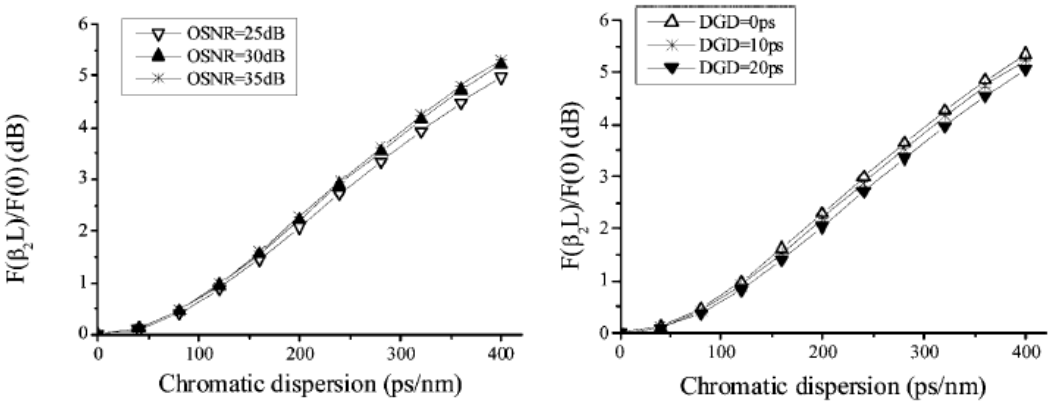

(a) (b)

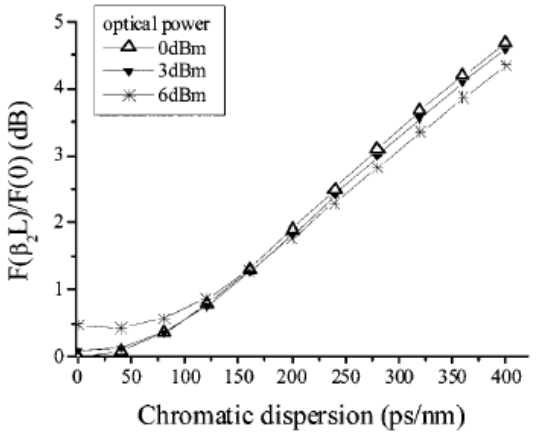

(c)

Fig. 2.8 Dependency of CD monitoring using RF spectrum on (a) OSNR (b) PMD (c) nonlinearity [18].

2.2 OPM using asynchronous amplitude histogram

Asynchronous amplitude histogram (AAH) basically depicts the statistics of the amplitudes of received signals. A sequence of signals is first asynchronously sampled at the receiver and AAH is obtained by plotting a histogram based on the samples. Shake *et al.* first proposed the use of AAH for OSNR monitoring by calibrating Q-factor derived from the histogram against OSNR [19]. As shown in Fig. 2.9, the AAH obtained from on-off keying (OOK) systems consists of two peaks-mark and space which corresponds to the logic "1" and logic "0" respectively. To quantitatively analyze the AAH, several parameters are derived from the statistics of the AAH peaks. $\mu_1(t)$, $\mu_0(t)$ $\sigma_1(t)$ and $\sigma_0(t)$ in Fig. 2.10 are the means and standard deviations of the two peaks against the eye diagram at time instant *t*. The distance between the two peaks is denoted by $\mu(t)$. Comparing the histograms in Fig. 2.9 and Fig. 2.10, it is obvious that the values of aforementioned parameters

change with the OSNR level. In the case of increased noise power as shown in Fig. 2.9, the two peaks are broadened and the values of $\sigma_1(t)$ and $\sigma_0(t)$ increase accordingly. If the OSNR is controlled by varying signal power as shown in Fig. 2.10, $\mu(t)$ and $\mu_1(t)$ will have dominant changes instead. Hence, it is possible to define a variable for the calibration of actual OSNR based on the distance between the peaks of AAH and their means and standard deviations.

In [19-21], Shake *et al.* defined a Q_{avg} as

$$Q_{avg} = \frac{\left|\mu_{1,avg} - \mu_{0,avg}\right|}{\sigma_{1,avg} + \sigma_{0,avg}} \tag{2.3}$$

where $\mu_{i,avg}$ and $\sigma_{i,avg}$ are the means and standard deviations of the mark and space level distributions. Since AAH contains samples from signal transitions in between the two peaks, the region of mark and space level distributions need to be specified before the calculation of $\sigma_{i,avg}$. An easy and common way of determining the mark and space level distributions is setting two boundaries, μ_{th0} and μ_{th1} which can be obtained from

$$\mu_{\text{th0}} = \mu_{0,\text{avg}} + \alpha\left|\mu_{1,\text{avg}} - \mu_{0,\text{avg}}\right| \tag{2.4}$$

$$\mu_{\text{th1}} = \mu_{1,\text{avg}} - \alpha\left|\mu_{1,\text{avg}} - \mu_{0,\text{avg}}\right| \tag{2.5}$$

where α is a value usually smaller than 0.5 and need to be empirically adjusted for optimum performance. AAH region beyond μ_{th1} is considered as mark level

distribution, whereas, the region below μ_{th0} is classified as the distribution of space level.

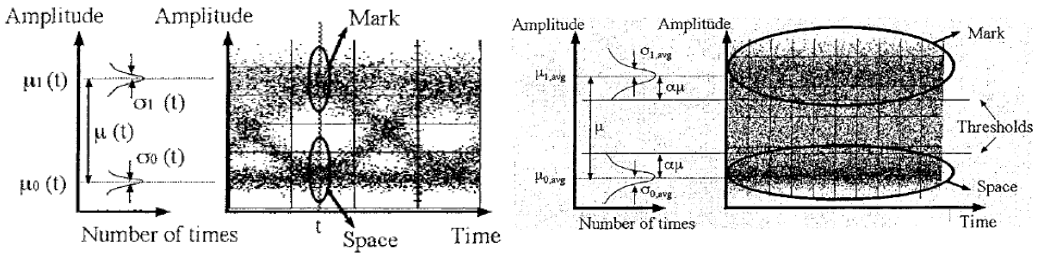

(a) (b)

Fig. 2.9 Comparisons between histograms and corresponding eye diagrams for different OSNR [21].

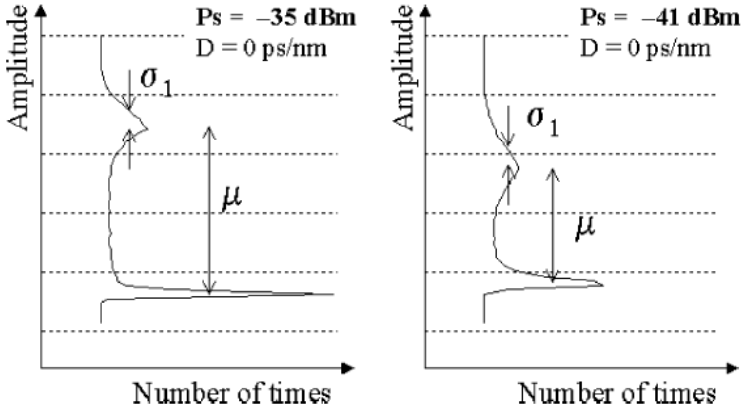

Fig. 2.10 Comparison of histograms for different OSNR changed by varying signal power [10].

A calibration graph of Q_{avg} against Q factor for different α is shown in Fig. 2.11 [21]. As can be observed from the graph, Q_{avg} has a clear one-to-one mapping relationship to each OSNR value. It is also noted that the calibration curve is dependent on α and its slope, which corresponds to the monitoring sensitivity, increases with decreasing α . However, according to Shake's study, a smaller α require more samples and equivalently, a longer sampling time window to

achieve sufficient statistical averaging for reliable calculation of $\mu_{i,avg}$ and $\sigma_{i,avg}$ calculations. In addition to α, the calibration curve in Fig. 2.11 also depends on the pulse rise time, optical bandpass filter following the optical amplifier, the bandwidth of the electrical filter at the receiver and other channel parameters that may induce waveform distortion to the signals. Thus, separate calibration graphs maybe required for each channel in practical systems.

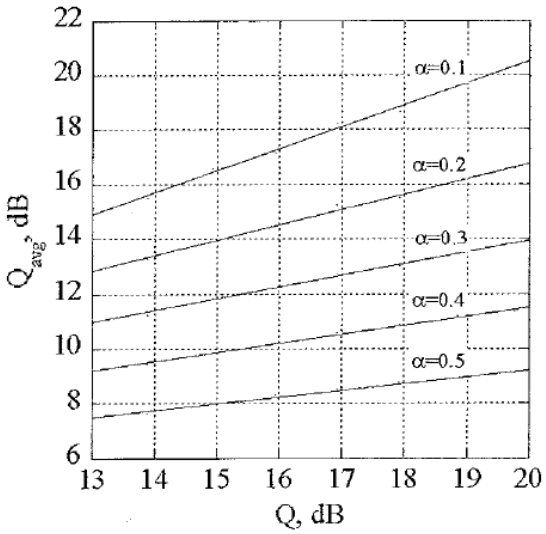

Fig. 2.11 Calibration graph of evaluated Q_{avg} against actual Q factor for different α [21].

Despite its sensitivity to channel configurations, AAH has attracted strong research interests ascribed to its low cost and easy implementation nature. Weinert *et al.* investigated the application of AAH to OSNR monitoring for RZ signals [22]. Studies of AAH-based OSNR monitoring for phase modulated signals are covered in [23]. In [24], the use of reference amplitude histogram (RAH) and optical pre-amplification is proposed to increase the OSNR monitoring sensitivity.

However, one remaining problem of AAH-based monitoring technique that requires future research is the isolation of different sources of signal degradation. As can be seen from Fig. 2.12 [10], the standard deviation of mark level σ_1 changes with the amount of accumulated CD which can be mistaken as OSNR degradation if no precaution is taken. To separate the source of signal degradation when both ASE noise and CD present, some new parameters are defined in [10], as shown in Fig. 2.13. $X_{\sigma 1}$ and X_{μ} are the ratio of increase in $\sigma_{1,avg}$ and $\left|\mu_{1,avg} - \mu_{0,avg}\right|$ to their reference values. Simulation results show that the summation of $X_{\sigma 1}$ and X_{μ} behaves differently when subject to either OSNR degradation or CD impairment. As can be seen from Fig. 2.14 [10], the value of $X_{\sigma 1} + X_{\mu}$ increases with the amount of accumulated CD, while it decrease when the signal power decreases. Therefore, by comparing the AAH obtained in a particular link to the reference AAH obtained when there is no CD, the source of degradation in signal quality can be identified based on the trend of changes in $X_{\sigma 1} + X_{\mu}$.

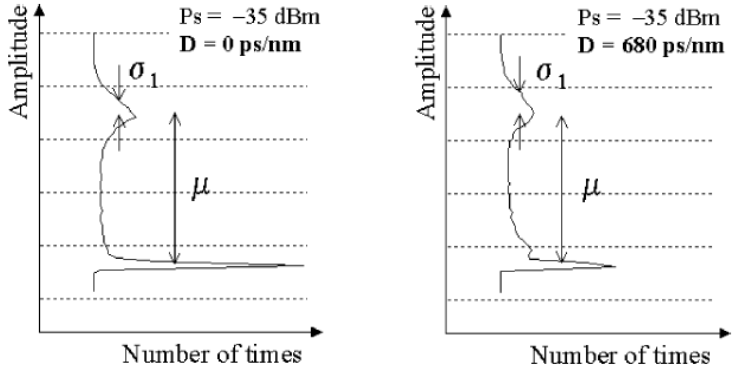

(a) (b)

Fig. 2.12 Dependence of asynchronous amplitude histogram on CD for 10 Gbps NRZ systems (a) Ps = -35 dBm, CD = 0 ps/nm and (b) Ps = -35 dBm, CD = 680 ps/nm [10].

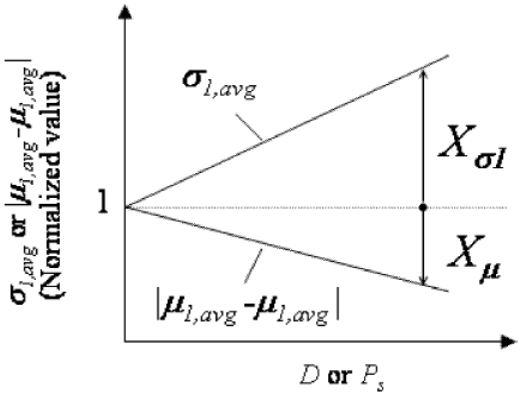

Fig. 2.13 Definition of $X_{\sigma 1}$ and X_{μ} [10].

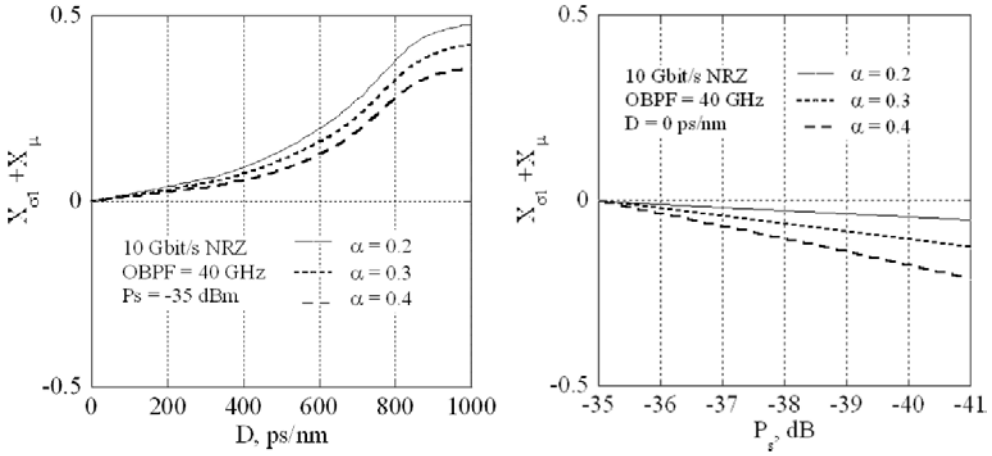

(a) (b)

Fig. 2.14 Dependence of $X_{\sigma 1} + X_{\mu}$ on (a) CD and (b) OSNR for 10 Gbps NRZ systems when α =0.2, 0.3 and 0.4 [10].

Later in [25], Li *et al.* proposed asynchronous amplitude histogram evaluation (AAHE) technique for simultaneous OSNR and CD monitoring in return-to-zero differential phase shift keying (RZ-DPSK) system. Assuming Gaussian pulse shape, the waveforms of pulse pair with π phase difference and 0 phase difference are shown in Fig. 2.15. When the phase difference is π, the intensity at A1 drops to zero because of the destructive interference between signals, whereas, constructive

interference enhances the intensity at A2 when the phase difference is 0. A plot of B, A1 and A2 against CD is given in Fig. 2.16. As can be seen from the graph, intensity at B drops monotonically with increasing CD, while intensity at A2 increases with CD. The two curves intersect at 500 ps/nm which could be the upper boundary of such CD monitoring technique, as the signal peak can no longer be identified.

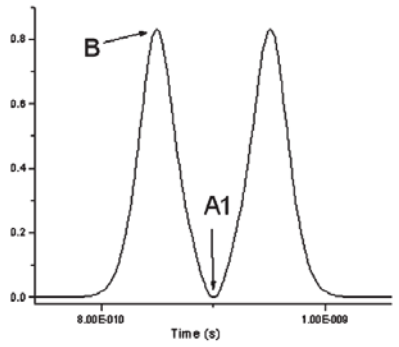

(a)

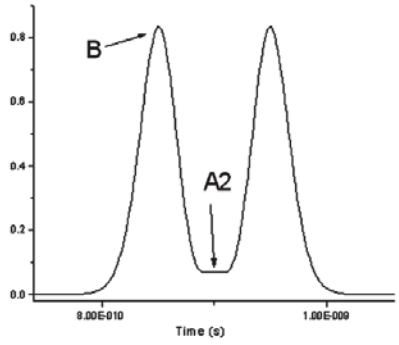

(b)

Fig. 2.15 Waveform of RZ-DPSK pulse pair with (a) π phase difference and (b) 0 phase difference [26].

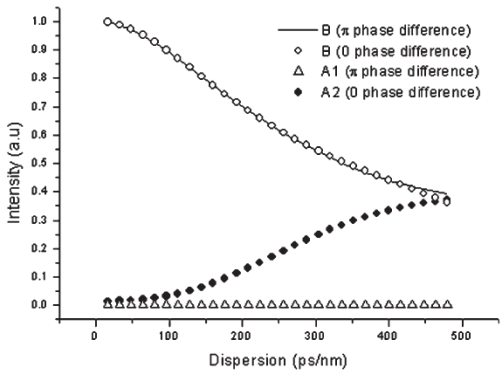

Fig. 2.16 Pulse pair intensity at point B, A1 and A2 for different CD [26].

Applying the analysis of Fig. 2.22 to the histogram of RZ-DPSK signal shown in Fig. 2.17, Li *et al.* found that the standard deviation of Peak 1 σ_1 does not vary much with CD but is sensitive to OSNR. Meanwhile, the mean value of Peak 1 μ_1 depends heavily on CD but is less sensitive to OSNR. Therefore, they defined the amplitude Q (AQ) and dispersion factor (DF) for the calibration of OSNR and CD respectively. The equations for evaluating AQ and DF are given by

$$\mathrm{AQ} = 10\log\left(\frac{P_0}{\sigma_1}\right) \tag{2.6}$$

$$\mathrm{DF} = \frac{\mu_1}{P_0} \tag{2.7}$$

where P_0 is the average power of RZ-DPSK signal. Experimental and simulation results for OSNR and CD monitoring using AAHE are given in Fig. 2.18. As shown in the figures, OSNR and CD monitoring are approximately independent of each other for OSNR larger than 20 dB and the monitoring accuracy is also high.

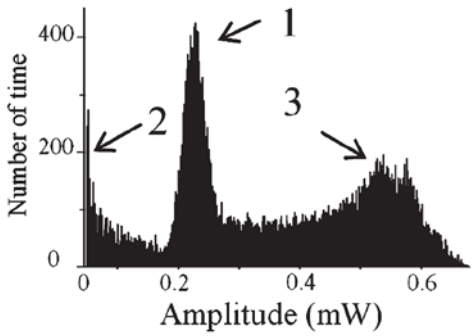

Fig. 2.17 Asynchronous amplitude histogram of RZ-DPSK signal [26].

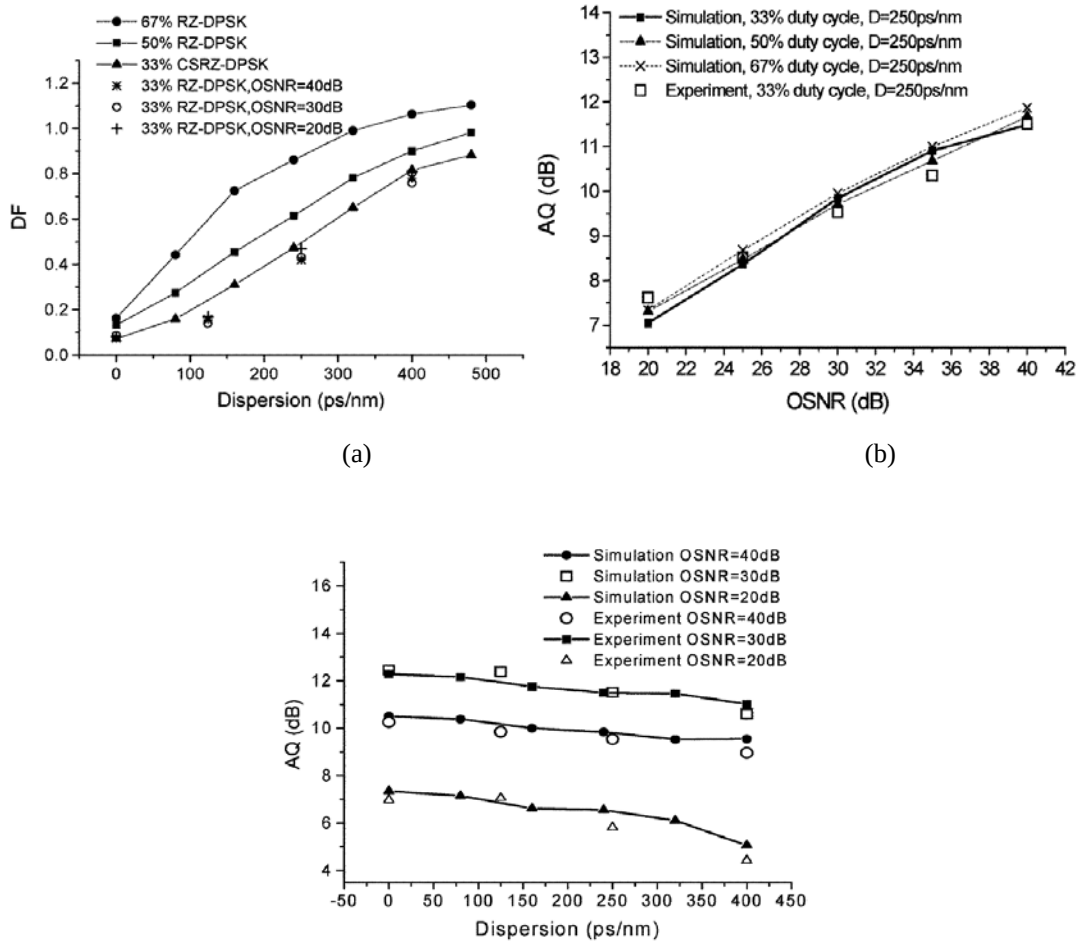

Fig. 2.18 Experimental and simulation results of (a) estimated DF versus CD. (b) estimated AQ versus OSNR (c) estimated AQ as a function of CD for different OSNR in RZ-DPSK system [25].

If polarization-mode dispersion (PMD) is also present in the RZ-DPSK system, it is proposed in [26] that CD information can be independently extracted using DF in Eq. 2.7 by controlling the signal to align with the two principal-state-of-polarization (PSPs) to minimize the effect of PMD. After the estimation of CD, the signal is realigned to a 45 degree with respect to PSP so that PMD effect can be maximized and monitored using a predefined factor DF2. The expression of DF2 is given by

$$DF2=\mu_2 / P_0 \tag{2.8}$$

where μ_2 is the mean value of Peak 2 in Fig. 2.18. Although μ_2 is also affected by CD, it can be solely used for calibration of PMD, as we have already obtained the value of CD in preceding process. Experimental and simulation results of PMD monitoring in presence of CD is given in Fig. 2.19.

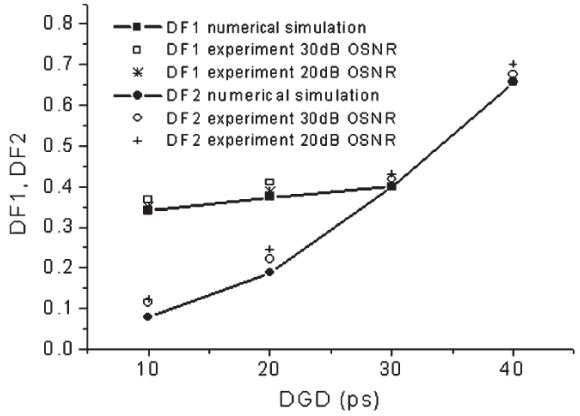

Fig. 2.19 Experimental and simulation results for PMD monitoring in RZ-DPSK system under 250 ps/nm chromatic dispersion [26].

2.3 OPM using artificial neural network

2.3.1 Artificial neural network

Artificial neural network (ANN) is a mathematical model that simulates the collective behavior among the interconnected neurons in the human brain. Generally, ANN consists of one input layer, one or more hidden layers, and one output layer. These layers are connected by weighting matrixes and each node inside hidden layer adopts an activated function which could be either linear or nonlinear. Fig. 2.20 [11] shows the typical structure of ANN.

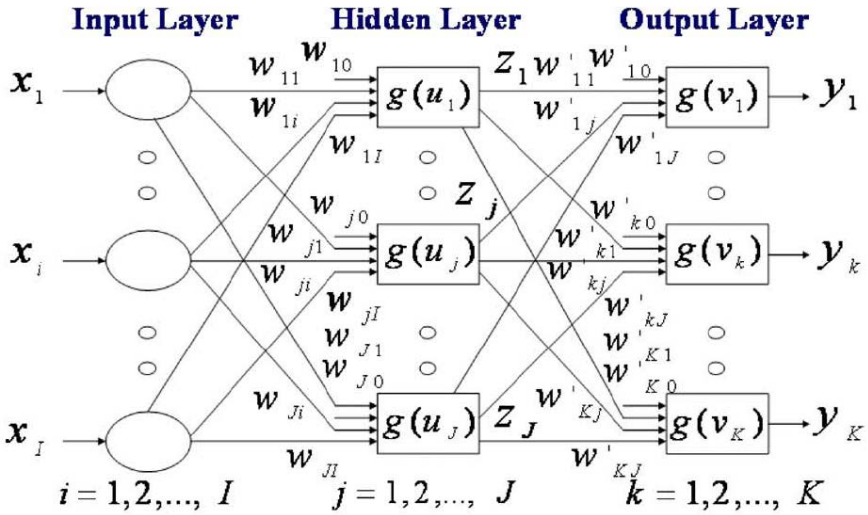

Fig. 2.20 Structure of a typical artificial neural network [11].

The weighting matrix that connects the input layer and hidden layer can be initiated by using either preloaded values or instantaneously generated according to prescribed rules. To smooth the mapping between the inputs and outputs, a process called training is required to adjust the weighting matrix. A sequence of input and output pairs are supplied to the ANN and optimization algorithms such as genetic algorithm automatically adjust the input and output weighting matrixes to minimize the difference between the outputs derived from the input variables and the expected

outputs. After the training process, another set of inputs are applied to the ANN and the calculated outputs are compared to the expected outputs for the verification of robustness and reliability of the trained ANN. This process is referred as testing.

In the case of optical performance monitoring, the outputs of ANN shall be the channel parameters to be monitored such as OSNR, CD and/or PMD. The inputs to the ANN actually can be arbitrary. However, the larger dependency of the input on the monitored channel impairments, the higher monitoring accuracy can be achieved. Hence, one of the main problems of ANN-based OPM is to find suitable inputs that are sensitive to various channel impairments in different manners. The tradeoff between monitoring sensitivity and range makes the selection of the input variables more challenging.

2.3.2 Review of OPM using ANN

Jargon *et al.* first proposed the use of ANN for simultaneous OSNR, CD and PMD monitoring [27] using eye diagrams. It is visually obvious from Fig. 2.21 that eye diagrams present distinct features depending on different impairment combinations. Therefore, using characteristics extracted from eye-diagram as the inputs to ANN, we should be able to monitor impairments that cause the distortions to eye-diagram. In [27], Jargon *et al.* chose the Q-factor, eye closure, jitter and crossing amplitude as the inputs to ANN with multilayer perceptron (MLP) structure and formed a training data pool by sweeping through OSNR from 16 to 32 dB (4 dB in step), CD from 0 to 60 ps/nm (15 ps/nm in step) and 0 to 10 ps (2.5 ps in step). To test the monitoring performance of the constructed ANN, another set of data consisting of the

impairment combinations of OSNR from 18 to 30 dB (4 dB in step), CD 7.5 to 52.5 ps/nm (15 ps/nm in step) and DGD from1.25 to 8.75 ps (2.5 ps in step) are also generated by numerical simulations. The monitoring outputs of the ANN for a 40 Gbps RZ-DPSK system are shown in Fig. 2.22.

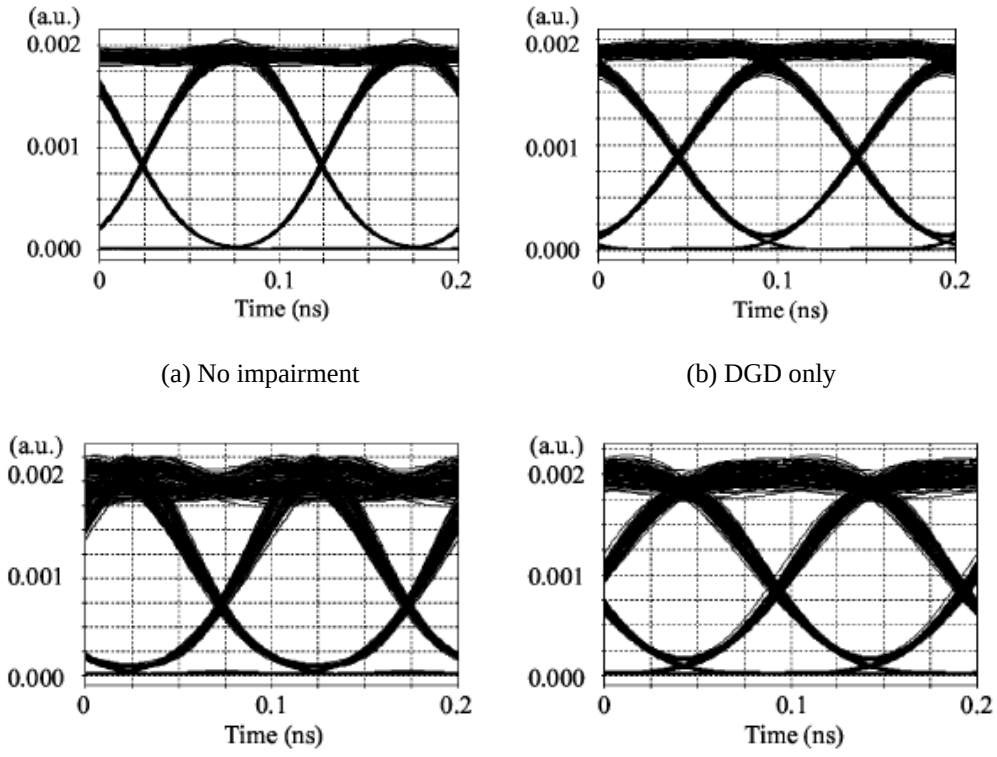

(a) No impairment (b) DGD only

(c) CD only (d) DGD and CD

Fig. 2.21 Eye diagrams of 10Gbps NRZ-OOK system with OSNR = 32 dB and various channel impairments (a) No impairment (b) DGD only (C) CD only and (d) DGD and CD [27].

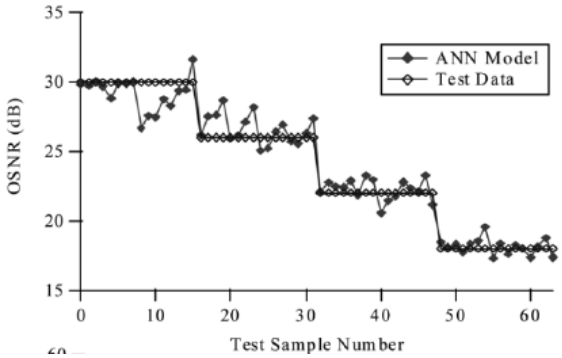

(a) OSNR

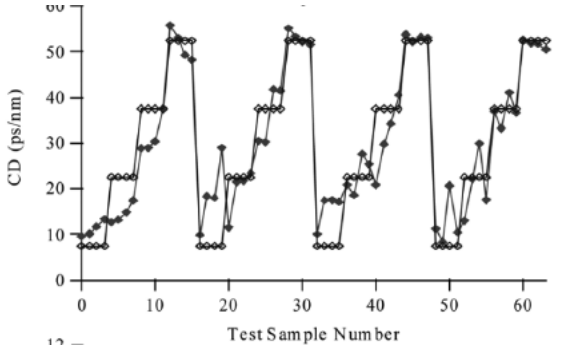

(b) CD

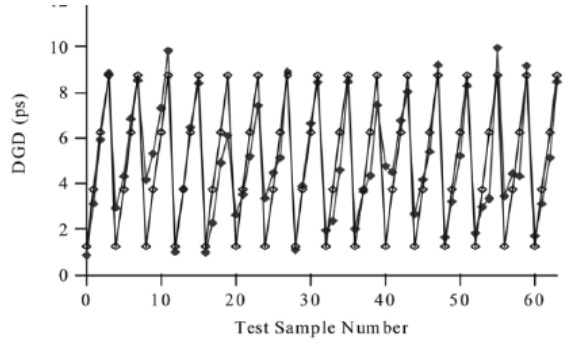

(c) DGD

Fig. 2.22 (a) OSNR (b) CD and (c) DGD monitoring results for 10 Gbps RZ-DPSK channel [27].

Recently, asynchronous constellation diagram (ACD) has also been proposed as an alternative input to ANN for OPM [28]. ACD is a 2 dimensional plot of asynchronously sampled in-phase (I) and quadrature (Q) components of the received signals. It is similar to the conventional constellation diagram but also shows

transitions between symbols. A set of ACD distorted by different impairment combinations is given in Fig. 2.23. Similar to eye diagrams, ACD also present distinguishable variations to a particular impairment combination. To make use of the asynchronous constellation diagram, the whole figure is divided into four quadrants as shown in Fig. 2.24. The means and standard deviations of the sample amplitudes in the first and third quadrants ($\overline{r_1}, \sigma_{r1}, \overline{r_3}, \sigma_{r3}$) are used as part of the inputs to ANN. In addition, the two interceptions of ACD on *y*-axis and another factor $Q_{31} = \left(\overline{r_3} - \overline{r_1}\right) / \left(\sigma_{r1} + \sigma_{r3}\right)$ are contained in the input vector to the ANN as well. The reason why only samples in the first and third quadrants are used is because the authors argue that the shape changes of ACD in these two quadrants are more obvious than that in the other two quadrants. Input variables derived from these two quadrants also provide better matching in monitoring performance between the training and testing data sets.

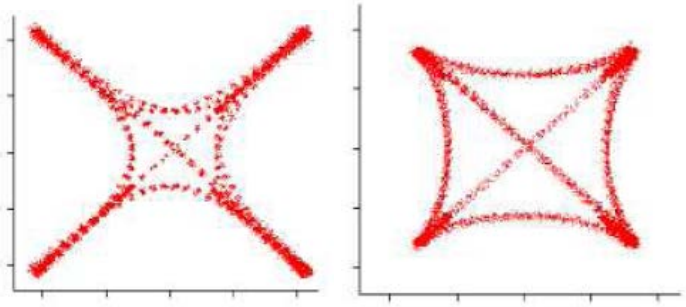

(a) None (b) DGD only

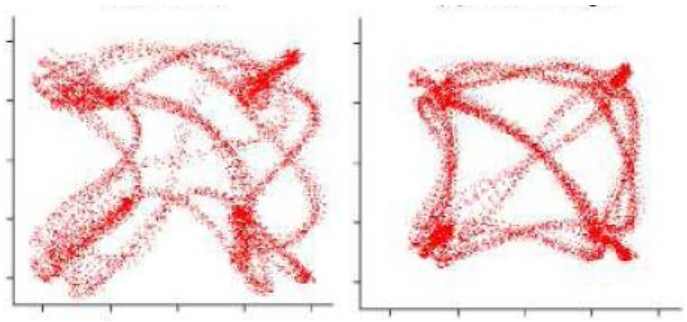

(c) CD only (d) DGD and CD

Fig. 2.23 Asynchronous constellation diagrams distorted by (a) None (b) DGD (c) CD and (d) DGD and CD [28].

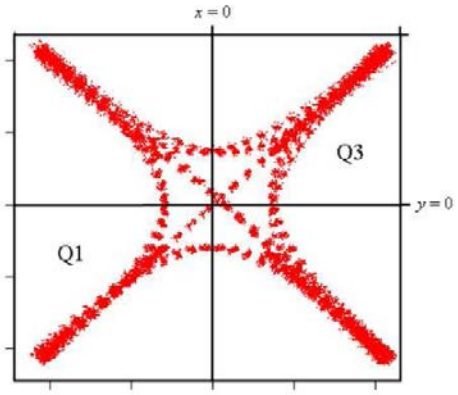

Fig. 2.24 Partitioned asynchronous constellation diagram for feature extractions for OPM using ANN [28].

The proposed technique was verified by simulations for 40 Gbps RZ-QPSK system. The impairment combinations for training are: OSNR – 12, 16, 20, 24, 28 and 32 dB; CD – 0, 40, 80, 120, 160 and 200 ps/nm; DGD – 0, 4, 8, 12, 16 and 20 ps. The impairment combinations for testing are: OSNR – 14, 18, 22, 26 and 30 dB; CD – 20, 60, 100, 140 and 180 ps/nm; DGD – 2, 6, 10, 14 and 18 ps. Fig. 2.25 shows the monitoring results and the RMS errors for OSNR, CD and DGD monitoring are 0.77 dB, 18.71 ps/nm and 1.17 ps, respectively.

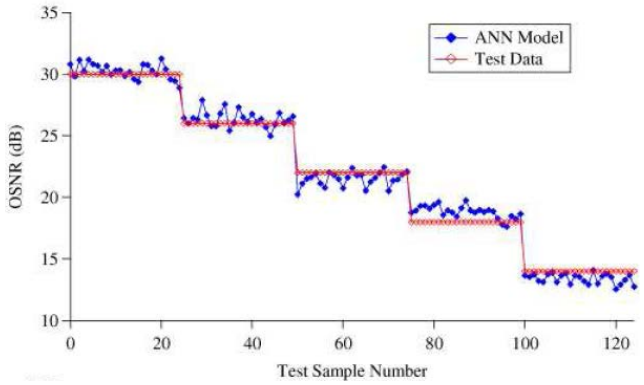

(a) OSNR

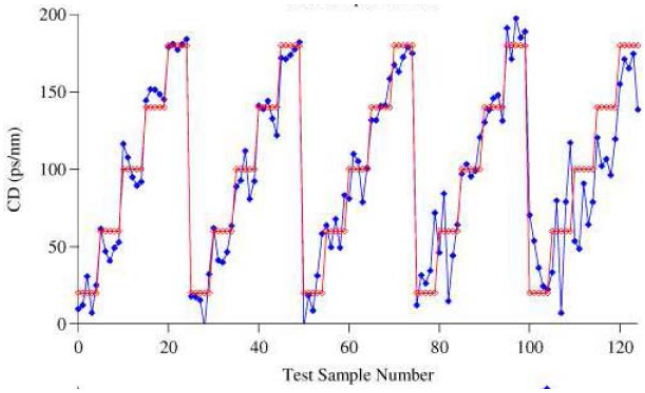

(b) CD

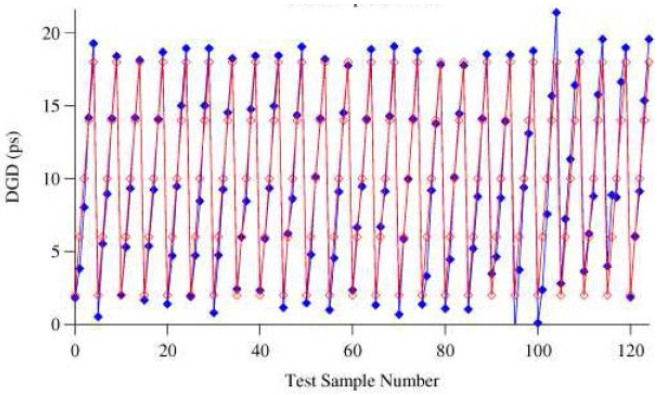

(c) DGD

Fig. 2.25 (a) OSNR (b) CD and (c) DGD monitoring results in 40 Gbps RZ-DQPSK system [28].

2.3.3 Other OPM techniques based on machine learning algorithm

In addition to ANN, the use of other machine learning techniquse such as pattern recognition for OPM is also studied in the literature [29]. Anderson *et al.* propose the use of joint probability density function (PDF) of a signal $x(t)$ and its delayed version $x(t+\Delta t)$, such pdf is also known as phase portrait in machine learning as the input to kernel-based ridge regression technique for the monitoring of OSNR, CD and DGD. A set of phase portraits distorted by various channel impairment combinations is shown in Fig. 2.26. The intensity of each pixel in the portrait represents the joint probability density. As can be seen from the graphs, both the shape of the phase portrait and its intensity distribution are sensitive to signal distortion and present distinct response to different channel impairments.

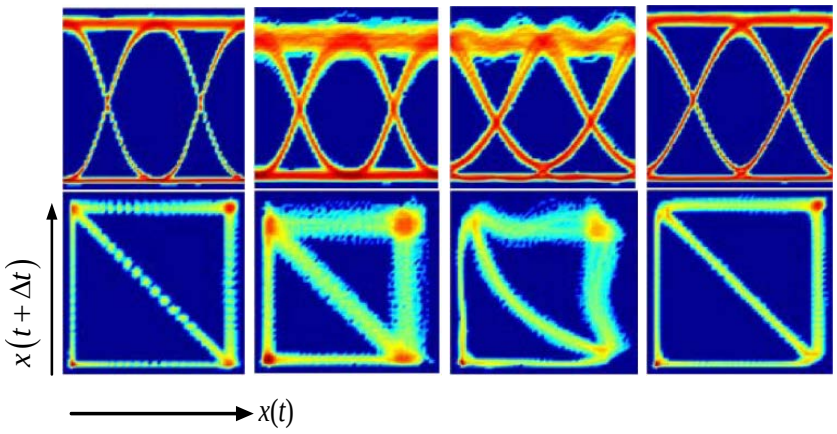

(a) Clean (b) ASE (c) CD (d) DGD

Fig. 2.26 Comparison of eye diagram and phase portrait for NRZ signal (a) OSNR = 35 dB and no impairment (b) OSNR = 25 dB (c) OSNR = 35 dB, CD = 800 ps/nm and (d) OSNR = 35 dB, DGD = 40 ps [29].

To evaluate the monitoring performance of the proposed technique for 40 Gbps NRZ-DPSK signals, a data pool consisting of 1700 different phase portraits is formed by simulating channel impairment combinations of OSNR from 13 to 26 dB

(2 dB in step), CD from 0 to 700 ps/nm (70 ps/nm in step) and DGD from 0 to 20 ps (5 ps in step). Since the signal state of polarization with respect to the fiber principal state of polarization (PSP) changes randomly during propagation, the quantity of effective DGD given by

$$\mathrm{DGD}_{\mathrm{eff}} = 4\gamma\left(1-\gamma\right)\mathrm{DGD} \tag{2.9}$$

is monitored instead of DGD, where γ is the split ratio of signal power between the two PSPs and it is randomly varied from 0 to 1 during the simulations. The simulation results of CD and $\mathrm{DGD}_{\mathrm{eff}}$ are shown in Fig. 2.27. The RMS errors of CD and $\mathrm{DGD}_{\mathrm{eff}}$ are 11 ps/nm and 0.75 ps, respectively.

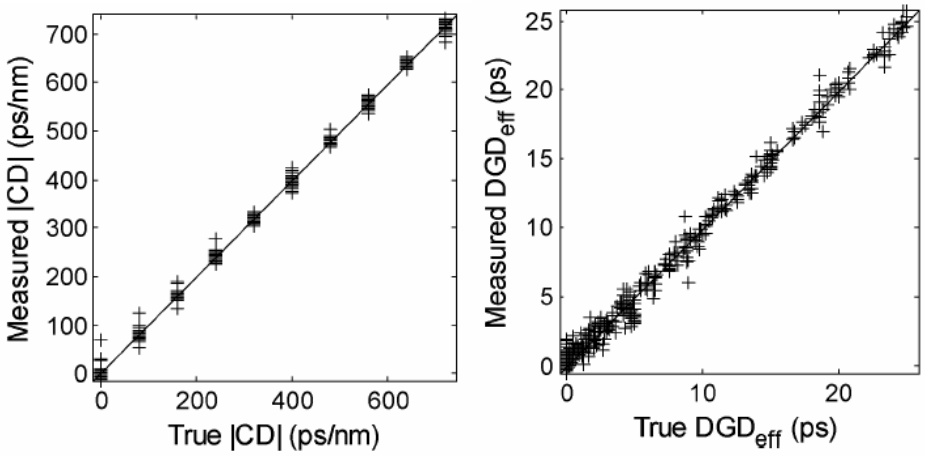

(a) (b)

Fig. 2.27 Simulation results of simultaneous monitoring of CD and $\mathrm{DGD}_{\mathrm{eff}}$ for 40 Gbps NRZ-DPSK signals [29].

2.4 OPM for coherent communication systems

2.4.1 Coherent optical communications

In coherent optical communication systems, information is modulated on both signal amplitude and phase. Since more bits are encoded in one symbol, the bandwidth efficiency of coherent systems is significantly improved compared to conventional IM/DD systems. To recover the phase of the optical signal for coherent systems, a 90 degree hybrid and a pair of balanced detector with single-ended photo-detection is proposed to extract the phase information as shown in Fig. 2.28. In this case, $E(t)$ and $E_{\mathrm{LO}}(t)$ denote the amplitude of the incoming signal and local oscillator, I and Q are the in-phase and quadrature components of the signal respectively.

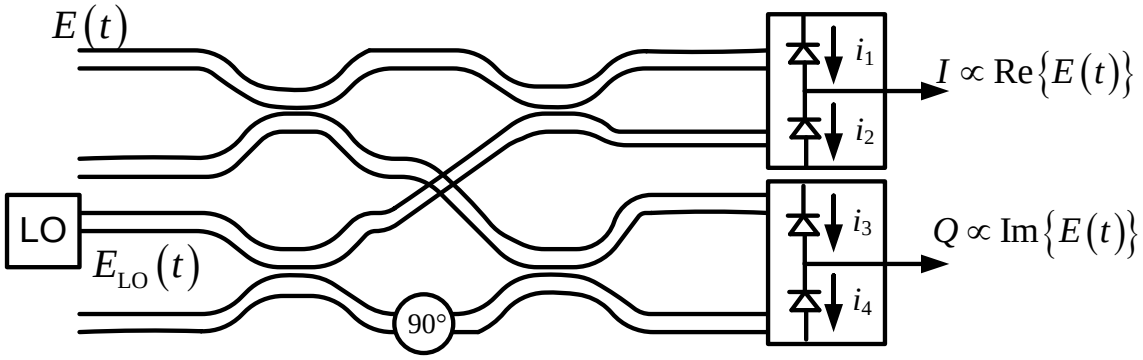

Fig. 2.28 Balanced detector for coherent receiver.

The photocurrent of photodiodes 1 and 2 can be expressed by

$$\begin{aligned} i_1 &= \frac{R}{2}\left|\left(E(t)+E_{LO}(t)\right)e^{j\omega_c t}\right|^2 \\ &= \frac{R}{2}\left[\left|E(t)\right|^2 + 2\,\mathrm{Re}\left\{E(t)E_{LO}^{*}(t)\right\} + \left|E_{LO}(t)\right|^2\right] \end{aligned} \tag{2.10}$$

$$\begin{aligned} i_2 &= \frac{R}{2}\left|\left(E(t)-E_{LO}(t)\right)e^{j\omega_c t}\right|^2 \\ &= \frac{R}{2}\left[\left|E(t)\right|^2 - 2\,\mathrm{Re}\left\{E(t)E_{LO}^{*}(t)\right\} + \left|E_{LO}(t)\right|^2\right] \end{aligned} \tag{2.11}$$

where R is the responsivity of the photodiode, ω_c is the carrier frequency and the symbol "*" denotes complex conjugate. The output of the first pair of balanced detector is then given by

$$\begin{aligned} I &= i_1 - i_2 \\ &= 2R\,\mathrm{Re}\left\{E(t)E_{LO}^{*}(t)\right\} \propto \mathrm{Re}\left\{E(t)\right\} \end{aligned} \tag{2.12}$$

Similarly, the output of the lower branch of the detector can be written as

$$\begin{aligned} Q &= i_3 - i_4 \\ &= 2R\,\mathrm{Im}\left\{E(t)E_{LO}^{*}(t)\right\} \propto \mathrm{Im}\left\{E(t)\right\} \end{aligned} \tag{2.13}$$

The phase of $E(t)$ can be easily obtained by calculating

$$\phi_s(t) = \tan^{-1}(Q/I) = \tan^{-1}\left(\frac{\mathrm{Im}\left\{E(t)\right\}}{\mathrm{Re}\left\{E(t)\right\}}\right) \tag{2.14}$$

2.4.2 Frequency offset estimation for optical coherent receiver

Calculation of Eq. 2.14 is based on the assumption that the frequencies of transmitter laser and local oscillator are identical. However, the lasing frequencies of the two laser sources are not necessarily identical to each other in practice. Let the frequency offset be $\Delta\omega$ such that the detected signal phase in Eq. 2.14 is modified to be

$$\phi_s'(t) = \phi_s(t) + \Delta\omega t \tag{2.15}$$

which increases linearly with time. It is argued that the frequency offset between the transmitter and receiver needs to be much smaller than the symbol rate to ensure the accuracy of phase estimation and data detection [30]. However, the frequency offset

in practical system can be as large as ±5 GHz [31]. Therefore, frequency offset estimation is necessary for maintaining the performance of coherent systems.

To this end, Zhang *et al.* in [32] proposed a two stage frequency offset estimator (FOE) algorithm whose implementation scheme is shown in Fig. 2.29. The first stage of the FOE utilizes the relationships between the maximum phase error output of Gardner algorithm and frequency offset to obtain a coarse estimation of frequency offset. Gardner algorithm is commonly used for the correction of timing phase error between the transmitter and receiver. In a coherent polarization multiplex (PolMux) PSK system with 2 times over-sampling rate, the phase error output of the Gardner algorithm in X-polarization state is given by

$$U_t(2k) = I_x(2k-1)\left[I_x(2k) - I_x(2k-2)\right] + Q_x(2k-1)\left[Q_x(2k) - Q_x(2k-2)\right] \quad (2.16)$$

where I_x and Q_x are the in-phase and quadrature samples of the received signal. By sweeping through the timing offset *t* or the number of sample delay *k*, an *S*-curve representing the estimated phase error $\widehat{U_t}$ caused by timing error can be traced out. Fig. 2.30 shows a series of *S*-curve for different frequency offsets.

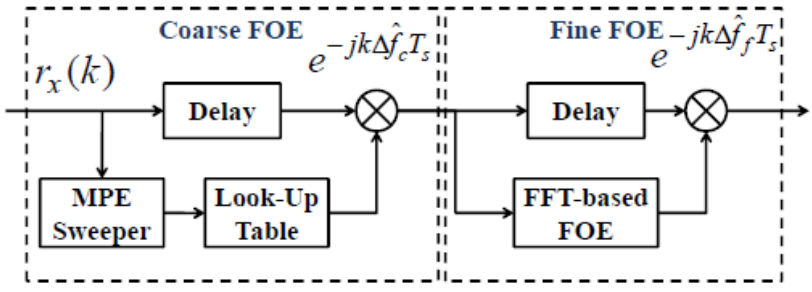

Fig. 2.29 Structure of a two-stage FOE [32].

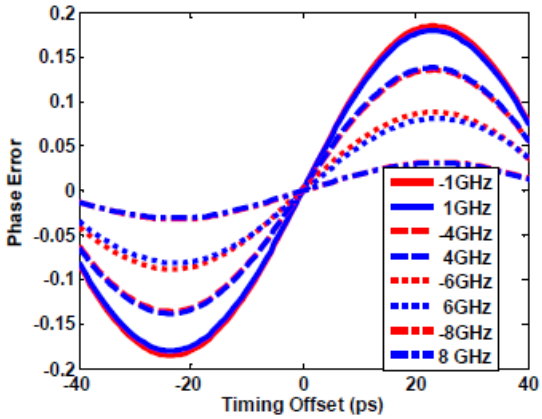

Fig. 2.30 Phase error output of Gardner algorithm versus timing offsets for different frequency offsets [32].

As can been seen from the figure, the maximal phase error (MPE) decreases (accuracy of timing error estimation decreases) when the laser frequency offset is increased. Such relationship can be used for FOE by constructing a look-up table of MPE at different frequency offsets. A plot of normalized MPE against frequency offset is shown in Fig. 2.31.

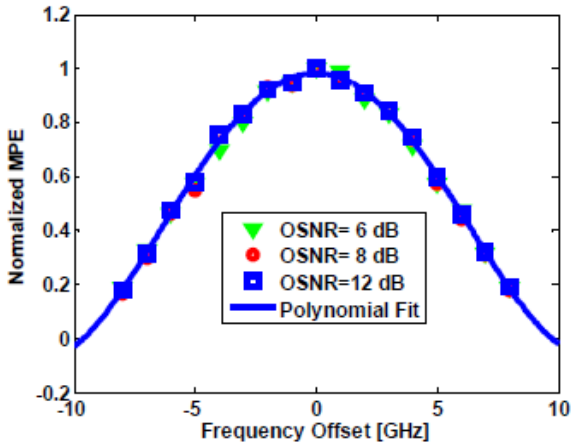

Fig. 2.31 Normalized MPE versus frequency offset for different OSNR [32].

The estimation error of frequency offset Δf_c after first stage coarse estimator is found to be within $\pm 1\,\text{GHz}$ which can be properly handled by a second stage fine FOE based on fast Fourier transform (FFT). Experiments are conducted to verify the proposed technique in a 42.8 Gbps PolMux RZ-QPSK system. The carrier wavelength is set to 1547.983 and the linewidth of the external cavity laser is about 100 kHz. The detailed experimental setup is given in Fig. 2.32. Fig. 2.33 shows the BER of the channel in presence of different frequency offsets, whereas a comparison of operation window of proposed technique and single stage FFT-based FOE is depicted in Fig. 2.34. It can be observed from Fig. 2.34 that by inserting the coarse FOE to estimate and compensate for the excessive Δf_c, the operation range of FFT-based FOE is significantly extended. Experimental results indicate that the technique proposed by Zhang *et al.* is able to monitor a frequency offset up to $\left[-0.5R_s,\ 0.6R_s\right]$ where R_s is the symbol rate.

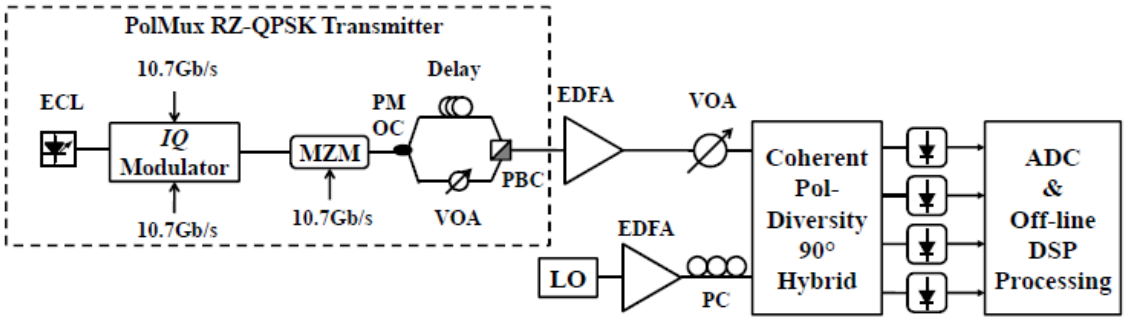

Fig. 2.32 Experimental setup of 42.8 Gbit/s PolMux RZ-QPSK system PMOC is the polarization-maintaining optical coupler. VOA is the variable optical attenuator. EDFA is the erbium-doped fiber amplifier and PC is the polarization controller [32].

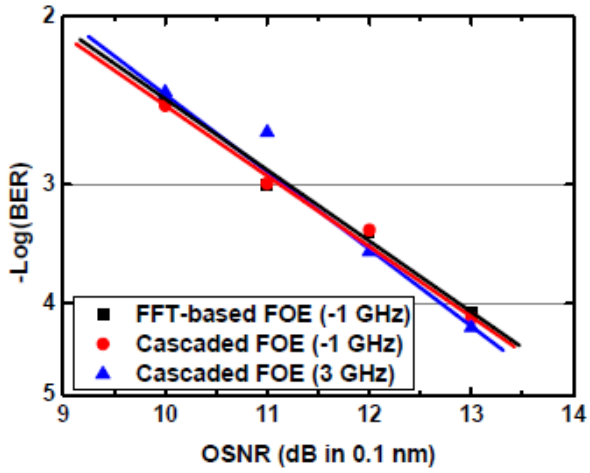

Fig. 2.33 BER performance of the experimental system using dual-stage cascaded FOE and FFT-based FOE for frequency offset at -1 GHz and 3 GHz [32].

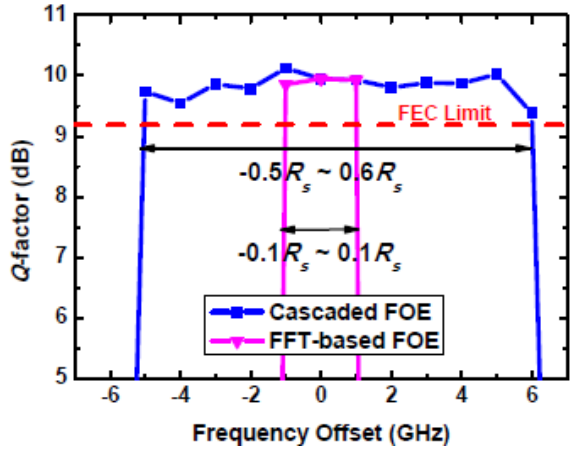

Fig. 2.34 Comparison of operation window of proposed dual stage FOE and FFT-based FOE [32].

One drawback of the above technique is that the data modulation needs to be removed before applying the second stage FOE which requires extra computation effort and hardware. In [33], Cao *et al.* proposed an alternative frequency offset estimation approach that makes use of the relationship between the spectrum of the received phase and the frequency offset.

Let the n^{th} received symbol be

$$S_n = I_n + jQ_n = \exp\left[j\left(\theta_{d,n} + \theta_{l,n} + 2\pi\Delta f n T_s\right)\right] + N_n \tag{2.17}$$

where $\theta_{d,n} \in \{-3\pi/4, -\pi/4, \pi/4, 3\pi/4\}$ is the modulated data phase for QPSK system. $\theta_{l,n}$ is the laser phase noise that can be modeled as a Wiener process. T_s is the symbol period and N_n represents the ASE noise. Assuming no ASE noise and laser phase noise, the corresponding argument of the signal can be expressed as

$$\begin{aligned} \varphi_{d,n} &= \theta_{d,n} + 2\pi\Delta f n T_s - 2\pi m \\ &= \left\langle \varphi_{d,n} \right\rangle + \theta'_{d,n} \end{aligned} \tag{2.18}$$

where m is an integer to control the value of $\varphi_{d,n}$ within the range of $[-\pi, \pi]$. $\left\langle \varphi_{d,n} \right\rangle$ and $\theta'_{d,n}$ are the mean and remaining values of $\varphi_{d,n}$. Fast Fourier Transform (FFT) on $\varphi_{d,n}$ gives

$$\mathrm{FFT}\left\{\varphi_{d,n}\right\} = \mathrm{FFT}\left\{\left\langle \varphi_{d,n} \right\rangle\right\} + \mathrm{FFT}\left\{\theta'_{d,n}\right\} \tag{2.19}$$

If the range of $2\pi\Delta f n T_s$ is ensured to be $\left[(2i-1)\pi/4, (2i+1)\pi/4\right]$, it can be calculated from Eq. 2.18 that

$$\begin{aligned} \left\langle \varphi_{d,n} \right\rangle &= \left\langle \theta_{d,n} \right\rangle + \left\langle 2\pi\Delta f n T_s \right\rangle - \left\langle 2\pi m \right\rangle \\ &= 2\pi\Delta f n T_s - 2\pi \left\langle m \right\rangle \\ &= 2\pi\Delta f n T_s - i\pi/2 \end{aligned} \tag{2.20}$$

Numerical results of Eq. 2.20 for different time interval *n* is plotted in Fig. 2.36. The solid line has a slope of $2\pi\Delta f$ and repeats itself periodically as expected. The reason why only one peak is observed in Fig. 2.35 is because the amplitude of harmonics

with order larger than one is buried in the flat noise. It is also noted that the phase shift caused by laser frequency offset $\arg\left[\exp\left(j2\pi\Delta fnT_s\right)\right]$ represented by the dashed line has a repeating period one fourth of that of $\left\langle \varphi_{d,n} \right\rangle$. Hence, to estimate the frequency offset, one can divide the frequency having the highest amplitude in phase spectrum by four. As the modulated data are randomly selected from the constellation, the signal phases are seen as flat noise after Fourier transform. On the other hand, the phase spectrum of the received signals contains peak components due to the periodic linear phase shift induced by frequency offset. Therefore, it is possible to extract the information about frequency offset without removing the modulated data by studying the phase spectrum of received signals. An illustration of the phase spectrum of QPSK signal with 0.5 GHz frequency offset is shown in Fig. 2.35. As can be seen from Fig. 2.35, the peak occurs at 2 GHz and the estimated frequency offset should be 0.5 GHz which agrees well with the actual value. Fig. 2.37(a) shows the block diagram of the proposed frequency offset estimation technique.

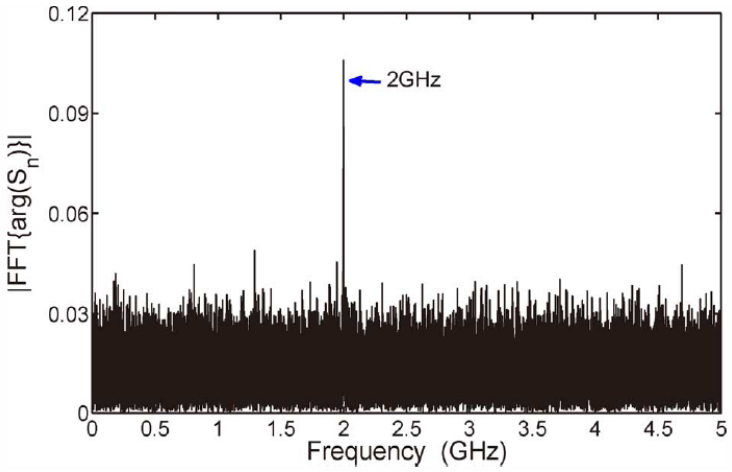

Fig. 2.35 Phase spectrum of the received QPSK signals with a frequency offset of 0.5 GHz [33].

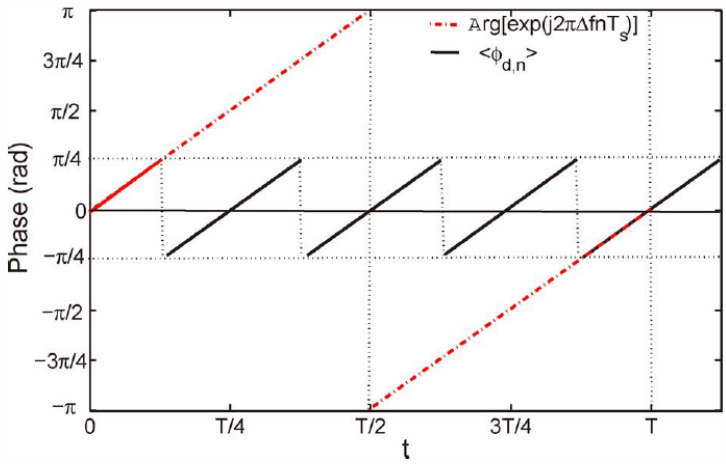

Fig. 2.36 $\langle \varphi_{d,n} \rangle$ and $\mathrm{Arg}\left[\exp(j2\pi\Delta f n T_s)\right]$ versus t for $\Delta f > 0$ [33].

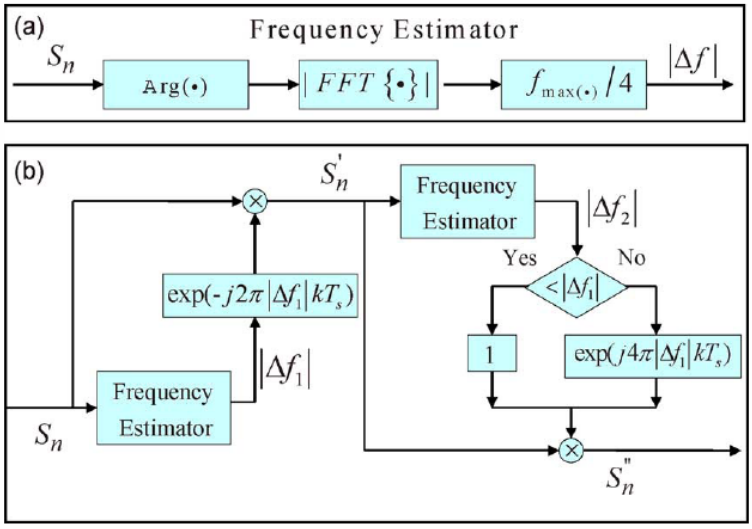

Fig. 2.37 Block diagram of proposed FOE (a) Estimator of frequency offset (b) Complete structure of FOE including estimation of the sign of frequency offset [33].

Although the absolute value of frequency offset can be extracted from the phase spectrum, the sign of frequency offset still remain unknown. To resolve this problem, Cao *et al.* introduce the second stage FOE as illustrated in Fig. 2.37(b). The absolute value of frequency offset $|\Delta f_1|$ is first obtained from the received signal using the technique discussed above. The sign of Δf_1 is then assumed to be positive and the input to the second FOE is obtained from

$$S_n^{'} = S_n \exp\left(-j2\pi|\Delta f_1|nT_s\right) \tag{2.21}$$

If the initial guess of the sign is correct, the output of the second stage FOE should be zero as the original frequency offset is already compensated by Eq. 2.21. Otherwise the value of $|\Delta f_2|$ will be $2|\Delta f_1|$.

To verify the performance of the proposed FOE, simulations are conducted for a 20 Gbaud QPSK system. The length of data sequence is 2^{15} and the laser linewidth is 100 kHz. The estimation errors of various frequency offsets in the range of [-2.4 GHz, 2.4 GHz] are plotted in Fig. 2.38. The impact of SNR on the estimation accuracy for 1 GHz frequency offset is studied and shown in Fig. 2.39 as well. As can be seen from the graphs, at 12 dB of OSNR, the maximum estimation error of frequency offset is less than 2 MHz. Although the performance of FOE is sensitive to SNR, such dependency can be mitigated by gathering more samples for phase spectrum calculation but at a cost of more computational complexity and time [33].

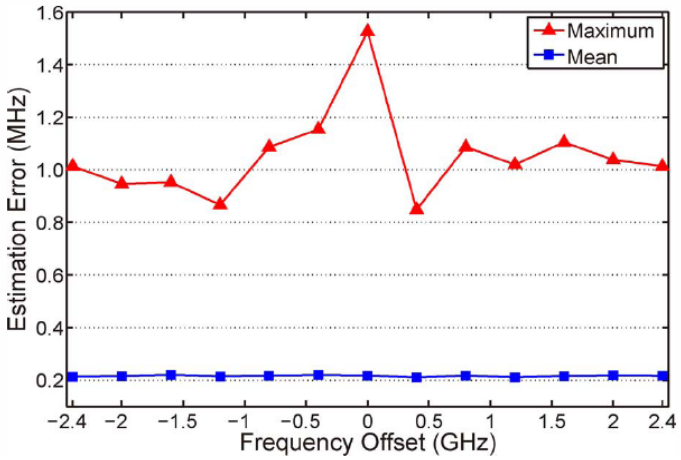

Fig. 2.38 Estimation error of frequency offset in the range of [-2.4 GHz, 2.4 GHz]. The SNR in electrical domain is 12 dB and 1000 independent trials are simulated for each frequency offset value [33].

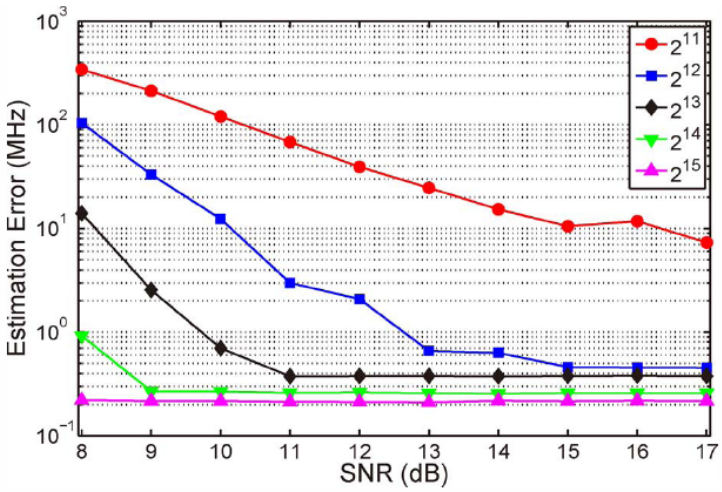

Fig. 2.39 Mean estimation error versus SNR for different sample size. The frequency offset is 1 GHz and 5000 trials are simulated for each SNR [33].

2.4.3 Laser linewidth monitoring in coherent optical communication systems

Laser phase noise induced by finite laser linewidth is a major concern in phase-modulated optical communication systems. Although the linewidth of commercially available external cavity lasers (ECL) and distributed feedback (DFB) lasers are in the order of kHz to several MHz respectively, the presence of laser phase noise at both the transmitting and receiving ends may still lead to carrier phase estimation error and symbol detection error. In addition, laser phase noise of the local oscillator can enhance the overall phase noise if accumulated CD is electronically compensated at the receiver [34]. Knowing the value of laser linewidth, the network management system can make more precise estimation of the overall phase noise within a particular channel for routing purpose and trigger fault alarms whenever the actual laser linewidth exceed prescribed thresholds.

Conventional techniques of laser linewidth estimation/measurement usually require the use of additional devices such as interferometer and RF spectrum

analyzer [35, 36]. Duthel *et al*. [37],. proposed a novel laser linewidth estimation technique by means of coherent detection. In particular, the time-variant phase $\varphi(t)$ at a coherent receiver can be obtained by

$$\varphi(t) = \arctan \frac{E_Q(t)}{E_I(t)} \tag{2.22}$$

where $E_Q(t)$ and $E_I(t)$ are the in-phase and quadrature components of the received signal. The instantaneous frequency $v(t)$ is then given by

$$v(t) = \frac{1}{2\pi} \frac{\partial \varphi(t)}{\partial t} \tag{2.23}$$

The spectrum of the frequency variation can be expressed as

$$F_{\mathrm{PSD}} = \left| \mathrm{FT}\left\{ v(t) \right\} \right|^2 \tag{2.24}$$

where FT represents Fourier Transform. Given finite bandwidth and limited number of samples in practical systems, F_{PSD} can be approximated as Rice distribution [37, 38], and the laser linewidth LW is

$$\mathrm{LW}=2\pi M_{Rice}^2 \tag{2.25}$$

where M_{Rice} is the mode of Rice distribution. The proposed technique is verified by simulations in the range of 100 kHz to 1 MHz. The frequency variation spectrum and its distribution with Rice fitting are shown in Fig. 2.40(a). To test the sensitivity of the technique to the modulation effect on laser frequency caused by laser control loop, a frequency modulation at 200 kHz is added as shown in Fig. 2.40(b). The

estimation results for both scenarios are shown in Fig. 2.41. It can be observed from the graph that the proposed technique can provide high accuracy monitoring in a wide range of laser linewidth. It is also noted by comparing the insets of Fig. 2.40(a) and (b) that the introduction of extra frequency modulation has little impact on the distribution of frequency variation and only results in a maximum 5% deviation at 1 MHz linewidth in Fig. 2.41.

Since the proposed technique only requires the information of the in-phase and quadrature components of the laser output which can be easily obtained in coherent systems, it can be used for in-service laser linewidth monitoring if the modulated signal symbols are known or recovered through other means.

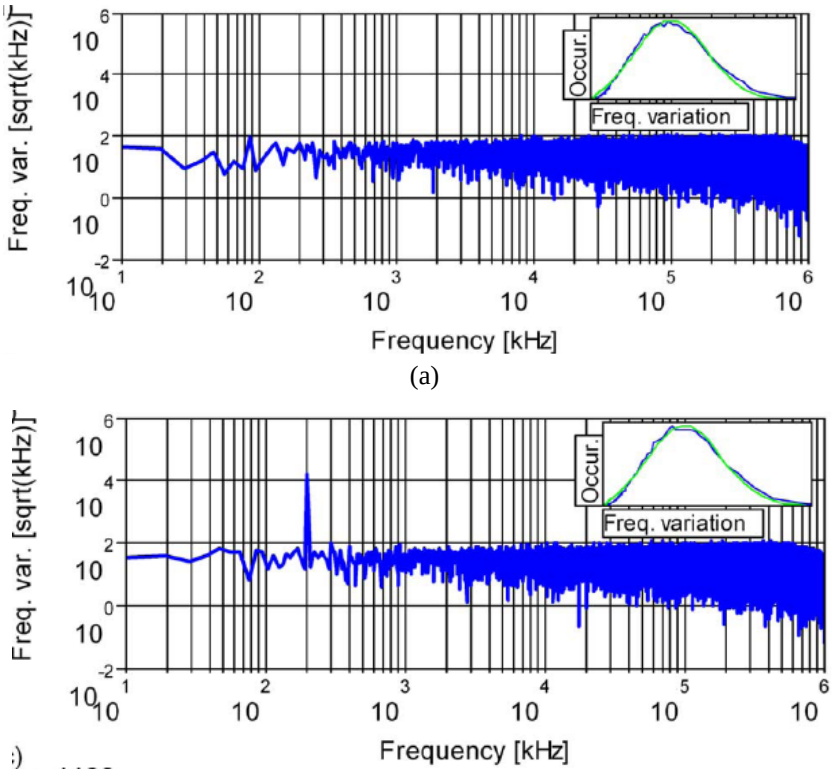

Fig. 2.40 Frequency variance spectrum (a) with modulation and (b) without modulation on laser frequency [37].

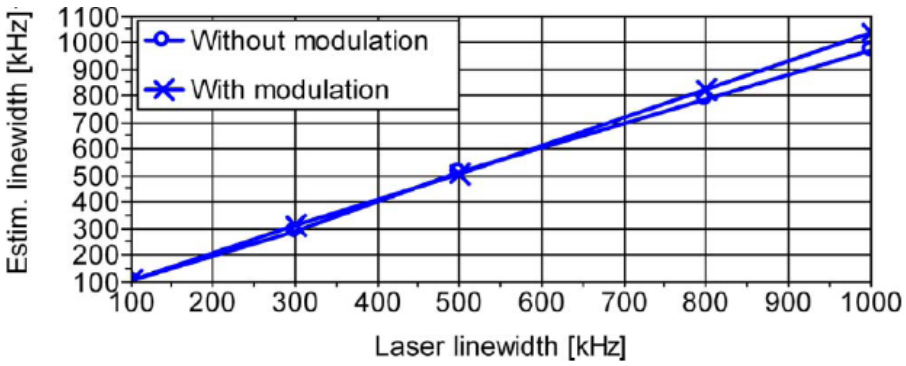

Fig. 2.41 Estimated linewidth versus true laser linewidth in the range of 100 kHz to 1 MHz [37].

2.4.4 Estimation of fiber Kerr nonlinearity

As the spectral efficiency increases with the advent of coherent detection, fiber Kerr nonlinearity can no longer be treated as a fundamental channel impairment to be avoided in coherent systems design, as they induce significant distortions to phase modulated signals and limit the maximum signal power that can be launched into the fiber. Various DSP-based techniques such as nonlinear phase noise compensation [14, 39], intra-channel four-wave mixing compensation [40] and digital back-propagation (BP) have been so far proposed to mitigate the nonlinear impairment. However, the performance of these techniques depends on the accurate knowledge of the fiber nonlinear parameter among others. The impact of inaccurate channel knowledge on the performance of BP is studied in Chapter 5.

Since fiber nonlinearity is simply avoided in older generation system designs, monitoring of fiber nonlinearity is not given as much attention as OSNR, CD and PMD monitoring previously. Little work has been done for nonlinear impairment monitoring in an optical communication link, though a few techniques have been proposed to measure the nonlinear coefficient of a short piece of fiber sample.

Kim *et al.* in [41] proposed estimation of fiber nonlinear refractive index n_2 by measuring the spectrum broadening caused by self-phase modulation (SPM). The nonlinear phase shift at the signal peak after propagating through the fiber sample is

$$\delta\phi = \frac{2\pi L}{\lambda}\frac{n_2 P_m}{A_{\text{eff}}} \tag{2.26}$$

where L is the fiber length, λ is the central wavelength of the light wave, P_{m} is the peak power of the signal, A_{eff} is the effective area of the fiber and n_2 is the fiber nonlinear refractive index. As $\delta\phi$ is time dependent, the phase shift caused by fiber nonlinearity, also known as Kerr effect, produces new frequency components which can be expressed by

$$\delta\omega = \frac{1}{2\pi}\frac{\partial\delta\phi}{\partial t} \tag{2.27}$$

The experimental setup used in the measurement is given in Fig. 2.42 and uncertainty of n_2 measurement is around $\pm 5\%$. As n_2 is sensitive to the polarization state, the measurement uncertainty can be as high as $\pm 10\%$ for certain types of fiber as reported in [41].

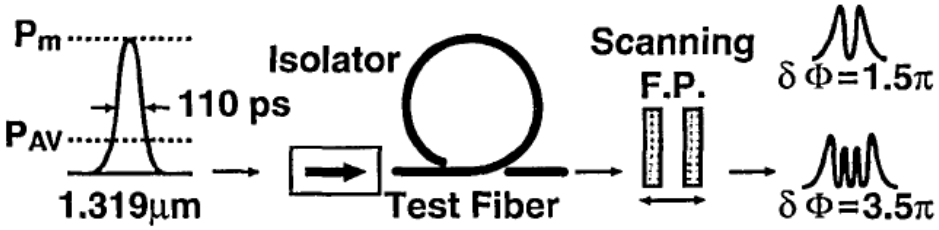

Fig. 2.42 Experiment setup for nonlinear refractive index measurement using SPM [41].

In addition to SPM, cross-phase modulation (XPM) can also induce spectrum broadening when two or more channels are present. A XPM-based n_2 measurement technique is studied in [42]. The phase shift $\delta\phi$ is modified to be

$$\delta\phi = \frac{2\pi L_{\text{eff}}}{\lambda}\frac{n_2}{A_{\text{eff}}}\left(P_{\text{probe}} + 2bP_{\text{pump}}\right) \tag{2.28}$$

where P_{probe} and P_{pump} are the probe signal power and pump power respectively and b is a scalar that depends on the polarization states of the probe signal and the pump lights. When the two light waves are linearly polarized and parallel to each other, b = 1 and XPM effect is maximized, whereas, $\delta\phi$ is minimized if b = 1/3 when probe and pump lights are linearly polarized and orthogonal to each other. The measurement setup using XPM is shown in Fig. 2.43. The wavelengths of both light sources are set to be 1550 nm. The power of the pump light is relatively stronger than the probe signal so that XPM dominates the spectrum broadening. Experimental results of the proposed measurement technique indicate good agreement with the measured fiber nonlinearity reported in other literatures.

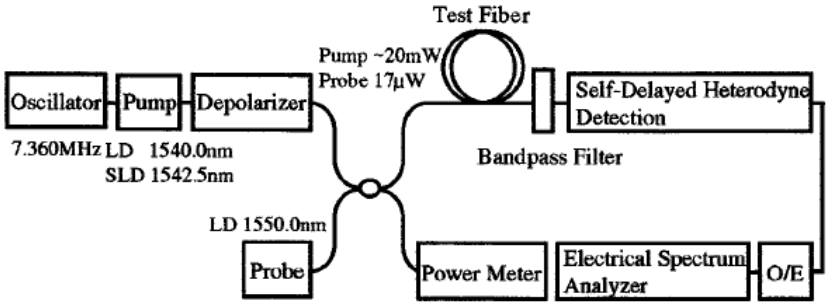

Fig. 2.43 Experiment setup for fiber nonlinearity measurement using XPM-based technique [41].

It should be noted that although the techniques discussed above are able to measure the fiber nonlinear coefficient accurately, they can only be applied to a short fiber sample in a well controlled experimental setup. Therefore, such techniques are only useful for fiber characterization purposes but not for Kerr nonlinearity monitoring of different types of deployed fiber in an optical network.

Chapter 3
OSNR MONITORING FOR HIGHER ORDER MODULATION FORMATS USING ASYNCHRONOUS AMPLITUDE HISTOGRAM

Although optical performance monitoring techniques based on asynchronous amplitude histograms have been extensively studied for OOK systems, little work has been conducted to investigate their performance in next-generation coherent optical networks using higher order modulation formats such as 16- and 64-QAM. In particular, the Q-factor defined in [19, 21] is no longer valid for modulation formats with three or more power levels. Using the statistics of single peak in [23] and [25] results in a relatively low monitoring sensitivity. The OSNR monitoring technique proposed in [24] requires a reference histogram for specific channel setup which may be difficult to obtain in large scale dynamic networks. It also remains unclear how the unique characteristics of AAHs of higher order modulation formats can help improve OPM in monitoring range and sensitivity.

To resolve the aforementioned problems, we propose AAH-based OSNR monitoring technique for 16- and 64-QAM systems by measuring the means and standard deviations of the highest two peaks of the AAH and calculate a parameter that can be used to calibrate against OSNR.

3.1 Operating Principles

Typical eye diagrams corresponding to received signals of a 16-QAM system are given in Fig. 3.1. The same set of received signals can also be asynchronously sampled to generate asynchronous amplitude histograms which are shown to the

right of corresponding eye diagrams. It is clear that the location of each peak in the histogram corresponds to a particular power level of the 16-QAM constellation and the spread of the peaks originates from signal-noise beating which depends on the OSNR of the channel.

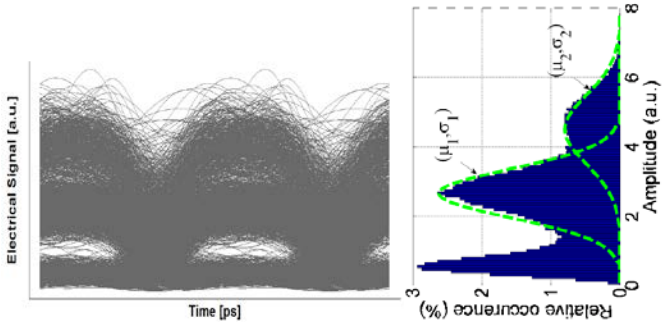

(a)

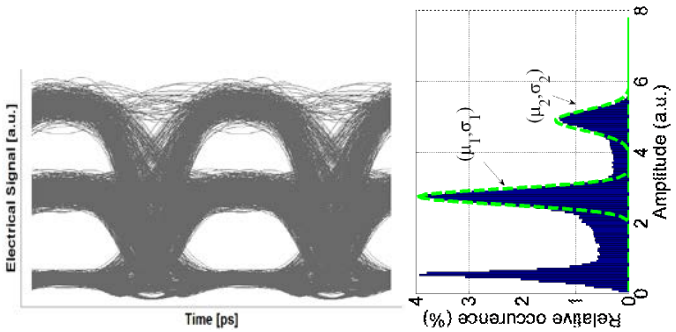

(b)

Fig. 3.1 Eye diagrams and corresponding asynchronous amplitude histograms for a 25 GSym/s NRZ-16-QAM system with (a) OSNR = 20 dB; (b) OSNR = 30 dB.

Let $S_k(t)$ be the k^{th} power level of the transmitted M-QAM signal (k = 1,2,3 for 16-QAM and k = 1,2,…,9 for 64-QAM) and $n(t)$ be the amplified spontaneous emission (ASE) noise introduced by inline optical amplifiers of the link. Neglecting the effect of shot noise and thermal noise at the receiver, the electrical current after photo-detection can be expressed as

$$I_k(t) = R\left(\left|S_k(t)\right|^2 + 2\,\mathrm{Re}\left\{S_k(t)n^*(t)\right\} + \left|n(t)\right|^2\right) \tag{3.1}$$

where R is the responsivity of the photodiode and is set to 1 for simplicity for the rest of the chapter. As *n(t)* is typically modeled as complex circularly symmetric Gaussian process, the mean of $I_k(t)$ is given by

$$\mu_k = \mathbf{E}\left[\left|S_k(t)\right|^2\right] + \mathbf{E}\left[\left|n(t)\right|^2\right] = P_{S_k} + P_N \tag{3.2}$$

where P_{S_k} and P_N are the received signal power of the k^{th} QAM signal level and ASE noise power respectively. The variance of $I_k(t)$ can be written as

$$\sigma_k^2 = \sigma_{S_kN}^2 + \sigma_{NN}^2 = 2P_{S_k}P_N + P_N^2 \tag{3.3}$$

where $\sigma_{S_kN}^2$ represents the variance of signal-noise beating and σ_{NN}^2 accounts for the variance incurred by noise-noise beating. By assuming that each peak is Gaussian distributed, we can approximate the locations and spreads of histogram peaks as μ_k and σ_k respectively which can be used for OSNR monitoring. In particular, we define a factor

$$F_{OSNR} = 20\log\frac{\mu_1\mu_2}{\sigma_1\sigma_2} \tag{3.4}$$

where μ_2 and σ_2 are the mean and standard deviation of the last peak (with the highest power) and μ_1 and σ_1 are the mean and standard deviation of the second last peak. Graphical illustrations of these variables are shown in Fig. 3.1 and Fig. 3.2 for

16-QAM and 64-QAM systems respectively. Theoretically, monitoring sensitivity can be maximized by using the means and standard deviations of all peaks as each of them interacts with ASE noise differently. However, as shown in Fig. 3.2, the number of identifiable histogram peaks for higher order modulation formats varies rapidly with OSNR and it may be difficult to extract all the peaks through simple curve fitting. Therefore, we choose to only use the means and variances of two peaks in defining F_{OSNR} as they always exist for any higher order modulation format and a wide range of OSNR. As the distributions of histogram peaks overlap with each other in general, they need to be appropriately separated so as to extract μ_k and σ_k. After smoothing the histograms with a simple moving average window, we isolate and mirror the right side of the last peak to its left to construct a Gaussian-like distribution from which μ_2 and σ_2 can be estimated. This distribution is then subtracted from the original histogram. Subsequently, the right side to the second last peak is similarly mirrored to the left side to obtain μ_1 and σ_1.

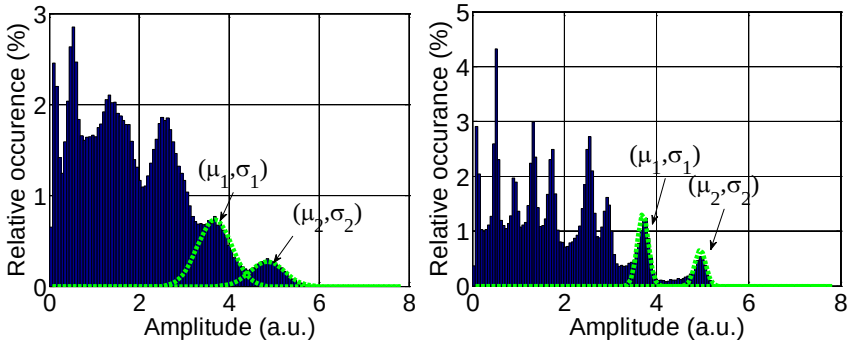

(a) (b)

Fig. 3.2 Asynchronous amplitude histograms for 25 GSym/s NRZ-64-QAM signals with (a) OSNR = 20 dB; (b) OSNR = 30 dB.

3.2 Simulation results and discussions.

The simulation setup for the proposed OSNR monitoring technique is shown in Fig. 3.3. A random symbol sequence modulated with either 16-QAM or 64-QAM format is transmitted at a symbol rate of 25 GSym/s. The erbium doped fiber amplifier (EDFA) adds ASE noise to the signal and the noise power is controlled by a variable optical attenuator (VOA) to realize different OSNR. CD and PMD impairments are simulated by the CD/PMD emulator. At the receiver, the signals are photo-detected and then asynchronously sampled at a rate that is much lower than the symbol rate.

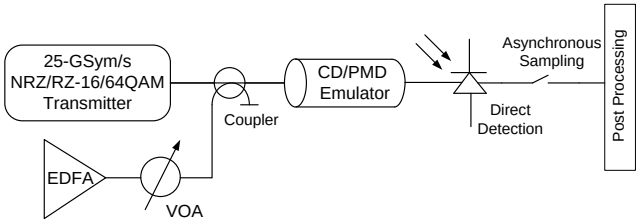

Fig. 3.3 Simulation setup for OSNR monitoring of 25 GSym/s NRZ/RZ 16/64-QAM signals.

In our simulations, 79438 samples obtained in commercial software VPI systems are used to generate each amplitude histogram. With the procedures described in the previous section, a series of F_{OSNR} for different OSNR values are calculated in Matlab and are shown in Fig. 3.4 to Fig. 3.7 for NRZ/RZ 16-QAM and 64-QAM systems together with their tolerance to CD and PMD.

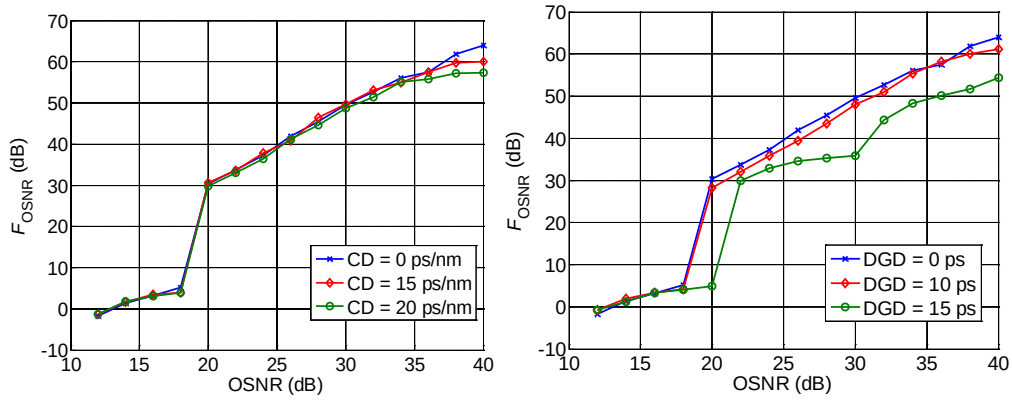

(a) (b)

Fig. 3.4 F_{OSNR} versus OSNR for a 25 GSym/s NRZ-16-QAM system with various levels of (a) CD and (b) PMD

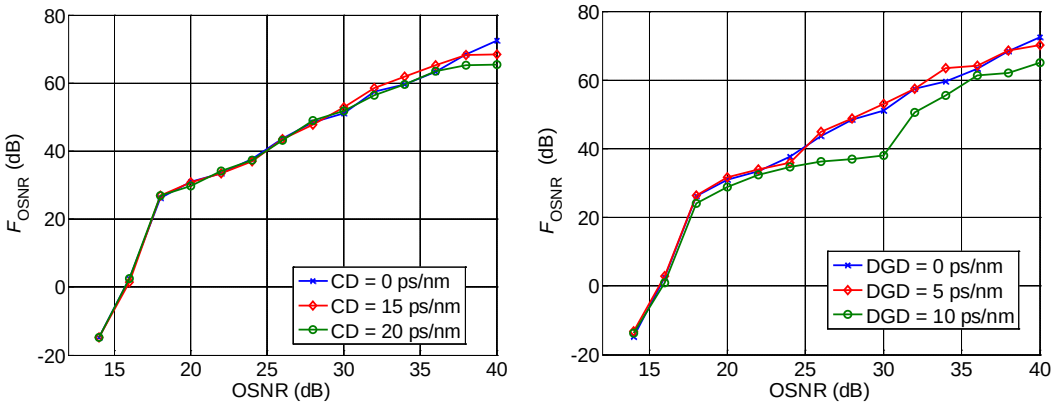

(a) (b)

Fig. 3.5 F_{OSNR} versus OSNR for a 25 GSym/s RZ-16-QAM system with various levels of (a) CD and (b) PMD.

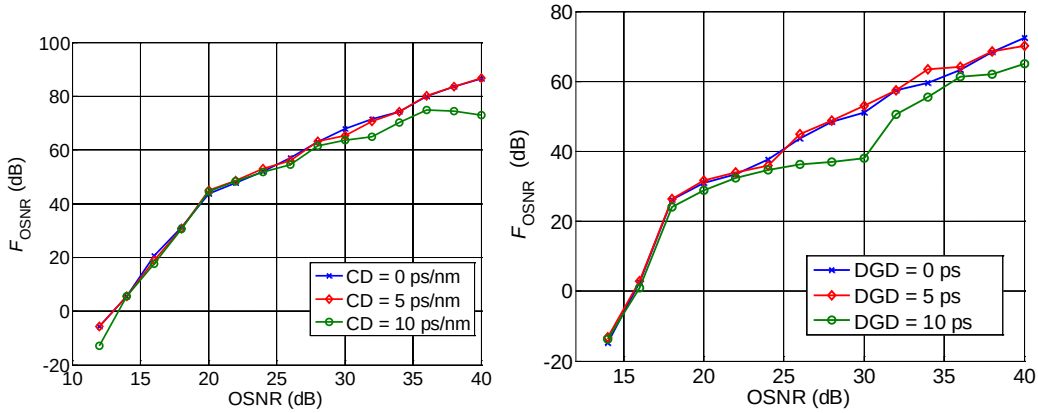

(a) (b)

Fig. 3.6 F_{OSNR} versus OSNR for a 25 GSym/s NRZ-64-QAM system with various levels of (a) CD and (b) PMD.

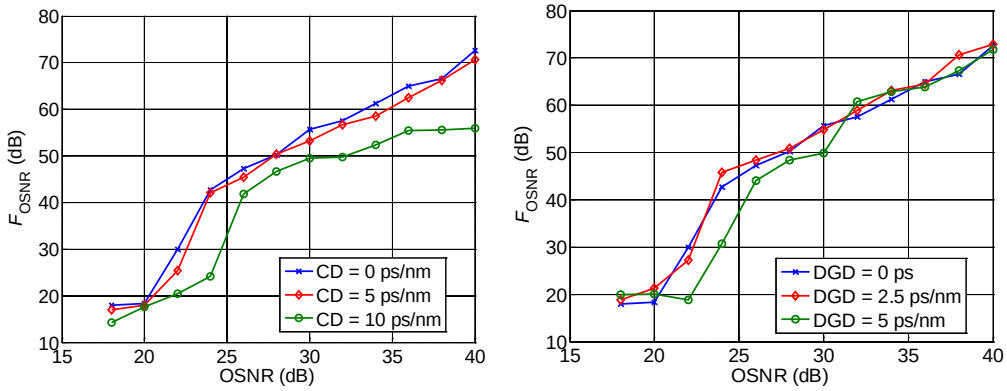

(a) (b)

Fig. 3.7 F_{OSNR} versus OSNR for a 25 GSym/s RZ-64-QAM system with various levels of (a) CD and (b) PMD.

As shown in the figures, F_{OSNR} has a one-to-one relationship with OSNR. The abrupt jump of F_{OSNR} in the low OSNR range is caused by the changes in the number of identifiable peaks from AAH. In addition, Fig. 3.4 shows that the proposed technique can tolerate around 15 ps/nm of CD and 10 ps of PMD in NRZ-16-QAM systems. For NRZ-64-QAM systems, the tolerance is about 5 ps/nm for CD and 5 ps for PMD according to Fig. 3.6. Meanwhile, Fig. 3.5 and Fig. 3.7 shows that the technique can tolerate 15 and 5 ps/nm of CD and 5 and 2.5 ps of DGD in RZ-16-QAM and RZ-64-QAM systems respectively. The lower monitoring boundary of the proposed technique is determined by the OSNR at which all peaks merged to a single peak where the proposed technique is no longer applicable. The smaller monitoring range and dispersion tolerance of RZ systems is partially ascribed to the increased signal bandwidth of the RZ pulses. Moreover, as the RZ pulse shape contains low-amplitude values regardless of the information symbols modulated on the pulse, its relative occurrence is much higher than other signal amplitudes. Therefore, compared to NRZ data, the occurrence of non-zero signal amplitudes are

considerably reduced for a given total number of samples and the histogram peaks merge much faster due to the finite number of samples and bin intervals used for generating AAHs. The reduction in tolerance level for 64-QAM formats compared with 16-QAM formats may be ascribed to its more compact and complex constellation. Finally, the average sensitivity of the proposed monitoring technique for 1 dB change in OSNR is more than 1.75 dB for all the modulation formats and is better than previously discussed AAH-based techniques.

3.3 Summary

In this chapter, we proposed the use of AAH to monitor OSNR for systems using higher order modulation formats such as 16-QAM and 64-QAM. To the best knowledge of the authors, this is the first work on OSNR monitoring for higher order modulation formats (16- and 64-QAM). The means and standard deviations of the last two peaks of the AAH are used to calculate a parameter that can be used to monitor OSNR. Simulation results demonstrated a wide monitoring range for both NRZ/RZ formats with monitoring sensitivities exceeding 1.75 dB for each dB change in OSNR. Since only the largest two peaks of the histogram are used to monitor OSNR, the proposed technique can be applied to any modulation formats with two or more power levels. Tolerance of the monitoring technique to CD and PMD is also studied.

Chapter 4
Optical Performance Monitoring Using Artificial Neural Network Trained with Asynchronous Amplitude Histograms

One disadvantage of AAH-based OPM techniques is that their monitoring results are sensitive to other channel impairments such as CD and PMD as shown in Fig. 3.4 to Fig. 3.7. Although further calibration can be used to mitigate such dependency, the low cost characteristics and flexibility of AAH-based monitoring techniques will be compromised. Furthermore, due to the extensive deployment of reconfigurable optical add-drop multiplexer (ROADM), it may not be possible to calibrate for each transmission link in dynamic optical networks. On the other hand, most existing AAH-OPM techniques are only designed to monitor one or two impairments simultaneously, and they usually require high OSNR to minimize the dependency of monitoring results on ASE noise [25]. Hence, extra effort is required to isolate and simultaneously monitor different channel impairments in practical OSNR range.

Recently, simultaneous channel impairment monitoring using machine learning techniques has been demonstrated in [27]. By supplying ANN and pattern reorganization algorithm with eye diagram [11, 27], asynchronous constellation diagram [28] or phase portrait [29], OSNR, CD and PMD can be monitored at the same time with large monitoring range and high accuracy. However, as discussed in previous section, the aforementioned machine learning based OPM techniques require high speed electronics for timing/clock recovery which significantly increase

the monitoring expenditure and make them unsuitable candidates for monitoring at intermediate network nodes where cost is a major concern.

Given all the facts above, we propose the combination of AAH and ANN for OPM that could possibly utilize the advantages of both techniques.

4.1 Principles of ANN using AAH

4.1.1 RBF neural network

Artificial neural network (ANN) is a mathematical model that simulates the collective behavior among the interconnected neurons in the human brain. The ANN adopted in this letter is radial basis function (RBF) neural network. Compared to other types of artificial neural networks, RBF has better approximation ability, simpler network structure, and faster learning speed. Generally, RBF contains an architecture consisting of three layers, namely input, hidden, and output layer. Each node inside hidden layer adopts a radial activated function, while nodes in the output layer implement a weighted sum of the outputs of all hidden nodes. A typical structure of multi-input and multi-output (MIMO) RBF neural network is shown in Fig. 4.1.

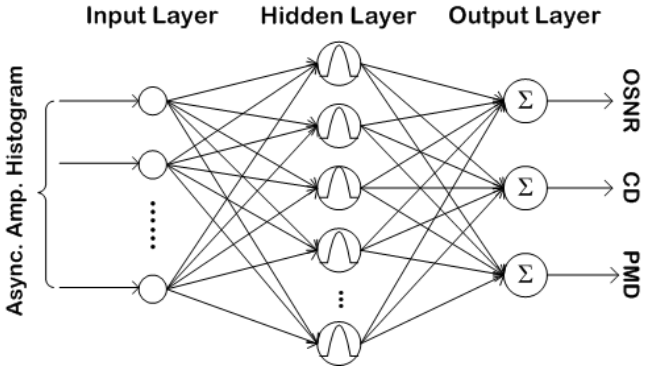

Fig. 4.1 Structure of a typical MIMO RBF neural network.

Theoretically, RBF neural networks can approximate any continuous functions defined on a compact set to any prescribed degree of accuracy by sufficiently expanding the neural network structure [43]. Furthermore, neural network training is usually carried out using randomly selected training subset [44] that enhances the robustness of the networks than using the predefined approach.

4.1.2 Asynchronous Amplitude Histogram

As discussed in Chapter 2, asynchronous amplitude histograms are basically the empirical distribution of received signal power and are sensitive to changes in OSNR, CD and PMD of the transmission link. Histograms obtained from 40 Gbps RZ-DQPSK signals distorted by selected combinations of transmission impairments are shown in Fig. 4.2.

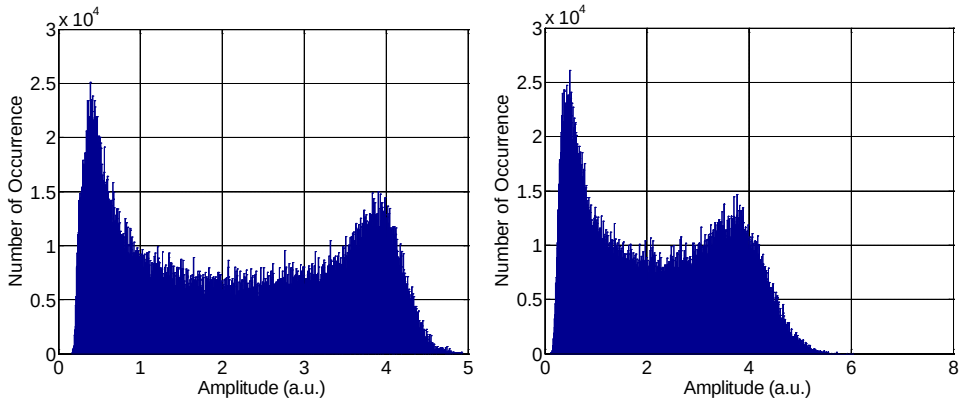

(a) (b)

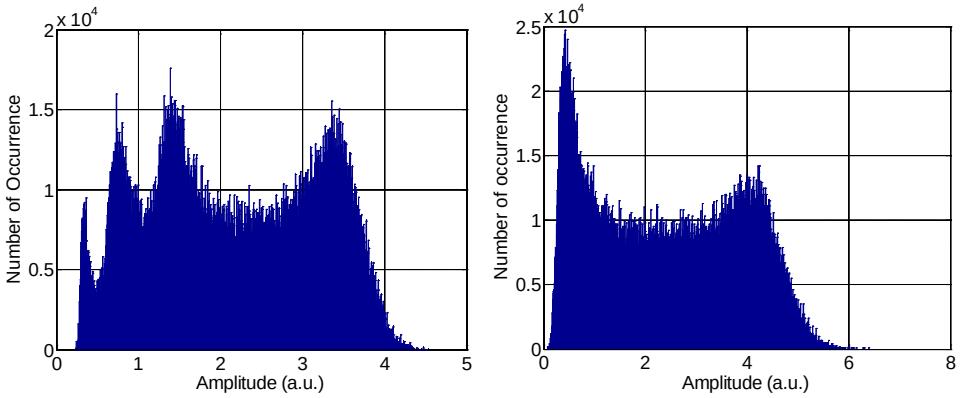

(c) (d)

Fig. 4.2 Asynchronous amplitude histograms obtained from 40 Gbps RZ-DQPSK signals distorted by selected combinations of transmission impairments: (a) OSNR = 30 dB, CD = 0 ps/nm, DGD = 0 ps; (b) OSNR = 24 dB, CD = 0 ps/nm, DGD = 0 ps; (c) OSNR = 30 dB, CD = 100 ps/nm, DGD = 0 ps; (d) OSNR = 30 dB, CD = 0 ps/nm, DGD = 10 ps.

It is visually obvious that different impairments cause different changes to the histograms. Existing AAH-based monitoring techniques usually model the histogram as a mixture of Gaussian distributions and parameters such as the means and variances of these Gaussians are used to calibrate against various channel impairments [21, 23]. However, as all these parameters are sensitive to channel impairments, they cannot be easily used for independent or joint monitoring of OSNR, CD and PMD. In contrast with extracting parameters form the AAH, the whole histogram itself contains information about the amount of different impairments in the system. Therefore, we can use the whole histogram represented by a vector of amplitude levels and corresponding occurrences as the ANN input neurons and the outputs of the ANN are the actual OSNR, CD and PMD values of the system. In our case, each histogram contains 100 bins. Thus, the number of input neurons is 200. Number of histogram bins to be used in practice depends on the monitoring accuracy, range and constraint on computational resources for real time

application. It needs to be found through continuous trials for each particular system.

4.2 Simulations Results and discussions

4.2.1 RZ-DQPSK Systems

The system configuration used in the simulations in VPI system is the same as shown in Fig. 3.3. A sequence of 40 Gbps RZ-DQPSK signals with 50% duty cycle is transmitted through a CD/PMD emulator. The erbium doped fiber amplifier (EDFA) adds ASE noise to the signal and the noise power is controlled by a variable optical attenuator (VOA) to realize different OSNR. At the receiver, the signals are photo-detected and then asynchronously sampled. The sampling rate can be much lower than the symbol rate. Collected samples are loaded into Matlab program for offline process.

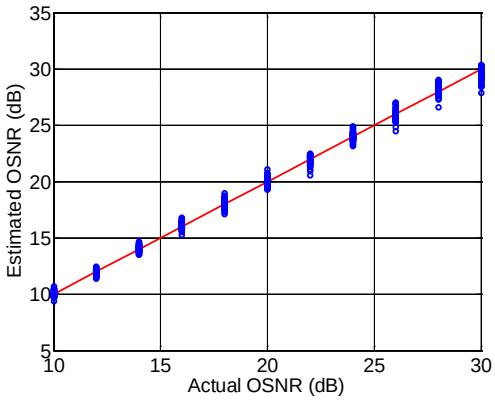

(a)

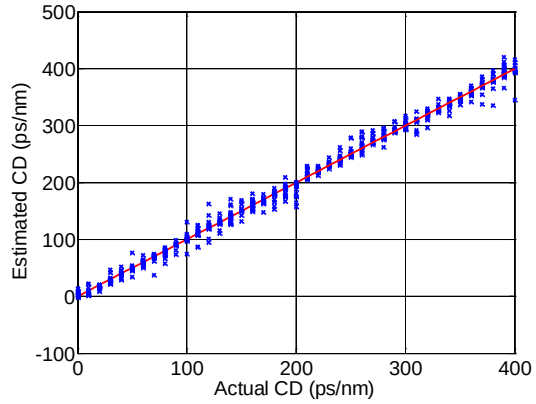

(b)

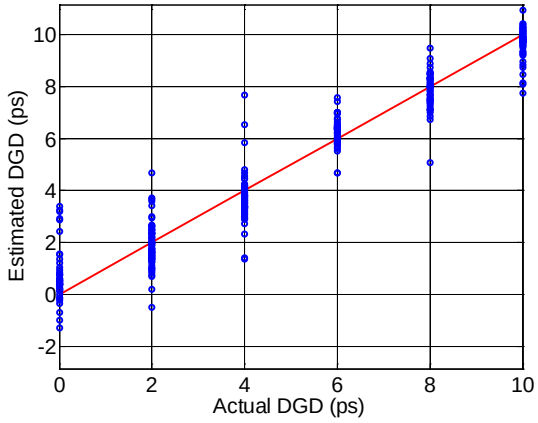

(c)

Fig. 4.3 (a) OSNR (b) CD and (c) DGD monitoring results for a 40 Gbps RZ-DQPSK system using ANN with AAH as inputs.

To demonstrate the proposed monitoring technique, we formed a pool of 2706 histograms by sweeping through OSNR values from 10 to 30 dB (in steps of 2 dB), CD from 0 to 400 ps/nm (in steps of 10 ps/nm) and DGD from 0 to 10 ps (in steps of 2 ps). 700 histograms are randomly chosen for testing and the rest are used as training data. The number of hidden neurons is optimized to be 326 using the incremental constructive method. The monitoring results for OSNR, CD and PMD monitoring are given in Fig. 4.3. As the testing results of ANN based technique

depend on the random selection of training data, 10 independent trials of random training and testing processes were conducted. The average RMS error is 0.45 dB, 9.82 ps/nm and 0.912 ps for OSNR, CD and PMD.

4.2.2 NRZ-16-QAM Systems

With the growing demand on transmission rates, advance modulation formats such as QAM has become increasingly popular for increasing spectral efficiencies. We also study the use of ANN trained with AAH for OSNR, CD and PMD monitoring for NRZ-16-QAM systems. The simulation setup is also similar to the one in Fig. 3.3, except that a NRZ-16-QAM transmitter is used instead. AAH obtained from simulations for selected combinations of transmission impairments are shown in Fig. 4.4. Again, each histogram exhibits distinct features corresponding to various impairments.

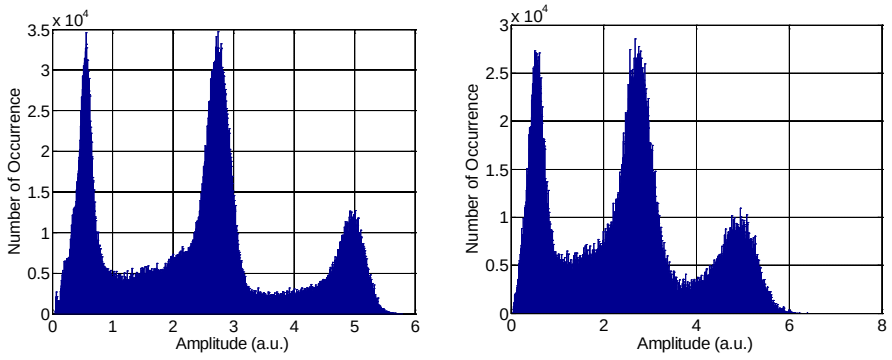

(a) (b)

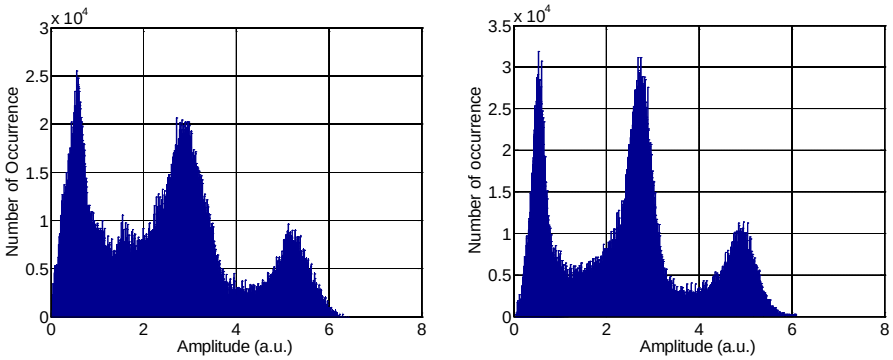

(c) (d)

Fig. 4.4 Asynchronous amplitude histograms obtained from 40 Gbps NRZ-16-QAM signals distorted by selected combinations of transmission impairments (a) OSNR = 30 dB, CD = 0 ps/nm, DGD = 0 ps; (b) OSNR = 25 dB, CD = 0 ps/nm, DGD = 0 ps; (c) OSNR = 30 dB, CD = 250 ps/nm, DGD = 0 ps; (d) OSNR = 30 dB, CD = 0 ps/nm, DGD = 10 ps.

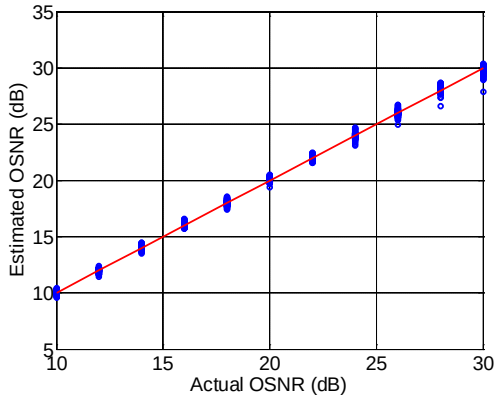

(a)

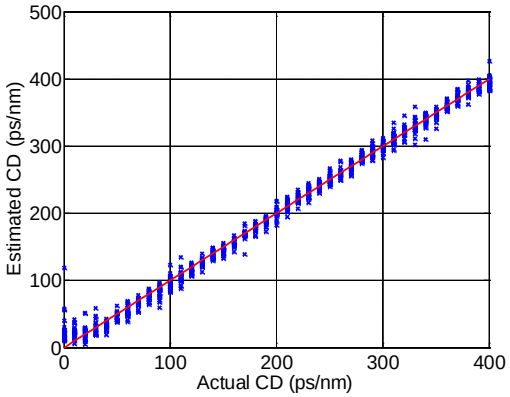

(b)

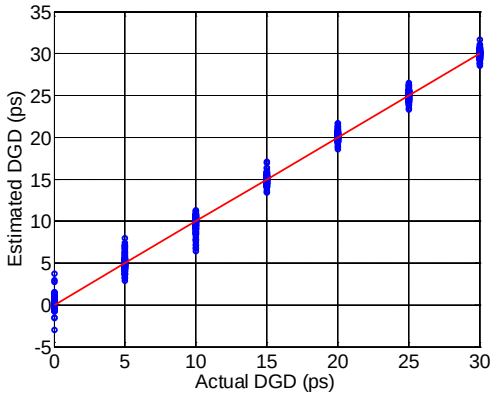

(c)

Fig. 4.5 (a) OSNR (b) CD and (c) PMD monitoring results for a 40 Gbps NRZ-16-QAM system using ANN with AAH as inputs.

We formed a pool of 3157 histograms by sweeping through OSNR values from 10 to 30 dB (in steps of 2 dB), CD from 0 to 400 ps/nm (in steps of 10 ps/nm) and DGD from 0 to 30 ps (in steps of 5 ps). 1000 histograms are randomly selected for testing and the rest are used for ANN training. The number of hidden neurons is optimized to be 287. Fig. 4.5 shows the testing results for OSNR, CD and PMD monitoring. The average RMS error for 10 independent trials of random training and testing is 0.2 dB, 9.66 ps/nm and 0.65 ps for OSNR, CD and PMD. The larger PMD monitoring range of NRZ-16-QAM signals may be ascribe to the fact that the symbol rate of NRZ-16-QAM is lower than that of RZ-DQPSK signals for a given bit rate which enables the histogram to identify larger PMD impairments before losing distinguishable characteristics.

4.3 Summary

In this chapter, we proposed the use of artificial neural network trained with asynchronous amplitude histograms as low-cost alternatives for accurate

simultaneous OSNR, CD and PMD monitoring which is not achievable by other monitoring techniques using asynchronous amplitude histogram alone. Simulation results obtained from both 40 Gbps RZ-DQPSK and NRZ-16-QAM systems demonstrate high monitoring accuracies with similar dynamic ranges compared to other known ANN based techniques. Since only received signal amplitudes are measured and no timing/clock recovery is required, the proposed technique will be applicable to different modulation formats with different symbol rates.

Chapter 5
SIMULTANEOUS AND INDEPENDENT MULTI-PARAMETER MONITORING AND FAULT LOCALIZATION FOR DSP-BASED COHERENT COMMUNICATION SYSTEMS

Contrary to older generation systems where nonlinearity is believed to be a fundamental impairment that system designers have to simply avoid, new impairment compensation techniques based on advanced DSP algorithms such as nonlinear phase noise compensation [14, 39], intra-channel four-wave mixing compensation [40] and digital back-propagation (BP) [15, 16] have been proposed to mitigate the effect of fiber nonlinearity-induced impairments. However, such techniques require detail knowledge of various parameters of the link including the nonlinear coefficients of fibers, number of spans N and the dispersion map (as supposed to just accumulated CD) of the link. Furthermore, as shown in Fig. 5.1(a), dynamic routing in practical terrestrial networks will still result in variations of link parameters such as N from time to time. To evaluate the performance impact with imperfect knowledge of the link, Fig. 5.1(b) shows the resulting Q-factor using BP with incorrect parameter values for a 1600 km system with 20 spans and 10% CD under-compensation per span. The modulation format is 200 Gb/s polarization-multiplexed NRZ-16QAM and the specifications of other link parameters are shown in Table 5.1 (in Section 5.2). The oversampling rate is 2 and the ξ parameter of the BP algorithm described in [15] has been optimized. The Q-factor corresponding to algorithms that only compensate for CD is also shown as reference. From the figures, it can be seen that when the number of spans used in BP is smaller than the

actual value by 3, the performance improvements by using BP is noticeably reduced. On the other hand, over-estimating N will be equivalent to BP with multi-span step size, which increases computational complexity [15]. Similarly, the fiber nonlinear coefficient γ needs to be monitored with good accuracy at the receiver in order to fully optimize the performance of BP. Although various techniques have been proposed for fiber nonlinear coefficients [41, 42, 45-47], there has been no means of direct estimation of fiber nonlinear coefficients in a communication system. Moreover, the value of N which is supposed to be given by upper layer protocols from the control plane, may not be always available.

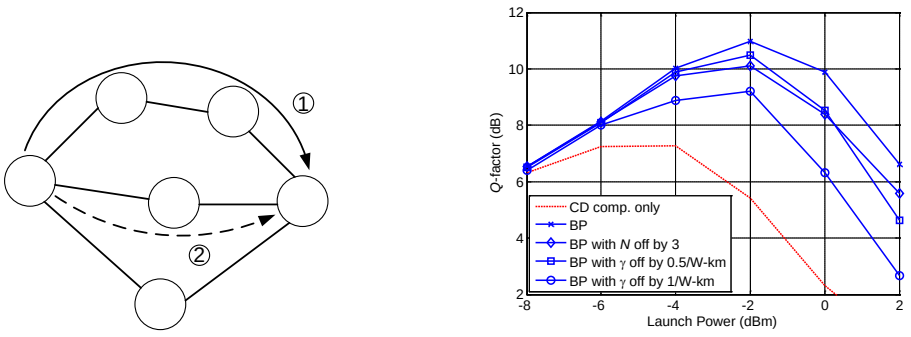

(a) (b)

Fig. 5.1 (a) In a dynamic optical network with ROADMs, signal may travel through different routes even for a given source and destination. This results in variations of the number of spans N as well as other parameters of the overall transmission link. (b) Q-factor vs. launch power for a NRZ-16-QAM system with length 1600 km and 10% CD under-compensation per span. System performance is sensitive to the accuracies of the parameters used in BP.

Since high order modulation formats used in next generation optical coherent network modulates information on signal phase, phase impairments caused by laser frequency offset between the transmitter (Tx) and local osciallator (LO), laser linewidth and ASE noise also need to be monitored for high QoS in addition to fiber

nonlinearity. In this chapter, we studied the use of pilot symbols with alternating power levels to jointly and independently monitor frequency offsets, laser linewidths, number of spans, fiber nonlinear coefficients as well as OSNR of the link. Analytical predictions are verified through simulation results for links with dispersion maps commonly used in practice. As the phase difference rather than the absolute phase of the received pilot symbols are monitored, the proposed technique should be robust against other phase-perturbing mechanisms that are slower than the sampling rate of the DSP. Finally, for a given link, we will show that by monitoring the changes in the variances of the received power and phase difference from time to time, one can locate faults or identify specific points in a transmission link with a sudden decrease in OSNR. Such fault localization technique has the advantage that no monitoring equipment is needed at intermediate nodes of the link.

5.1 Operating Principles

5.1.1 System model

Consider a coherent optical communication system consisting of N spans of single-mode fiber (SMF) with length L_S followed by a dispersion compensating module with 2-stage amplifiers and dispersion compensation fibers (DCF) of length L_D as shown in Fig. 5.2. The gain of amplifiers exactly compensates for the fiber loss in the previous span. The received signal passes through balanced detectors where the in-phase and quadrature outputs are sampled and processed in a DSP unit. To monitor various channel parameters, a sequence of pilot symbols with period T and alternating power levels P_1 and P_2 as shown in Fig. 5.3 is sent into the link prior to

data transmission. The symbol rate $1/T$ will be chosen such that the effect of chromatic dispersion (CD) and polarization-mode dispersion (PMD) is negligible. Let $n_{S_i}(t)$ and $n_{D_i}(t)$ be the amplified spontaneous emission (ASE) noise from optical amplifiers following the SMF and DCF of the i^{th} span respectively which are zero-mean complex circularly symmetric Gaussian random processes with power spectral density

$$S_{S(D)}(f) = n_{sp} h\nu \left(e^{\alpha_{S(D)} L_{S(D)}} - 1 \right) \tag{5.1}$$

where n_{sp} is the spontaneous emission factor, ν is the carrier frequency, $\alpha_{S(D)}$ is the attenuation coefficient of the SMF (DCF) and h is the Planck constant.

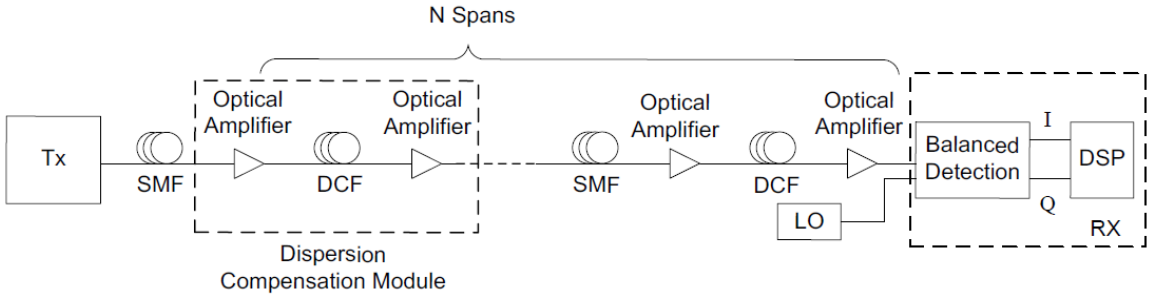

Fig. 5.2 A coherent communication system setup with optical CD compensation

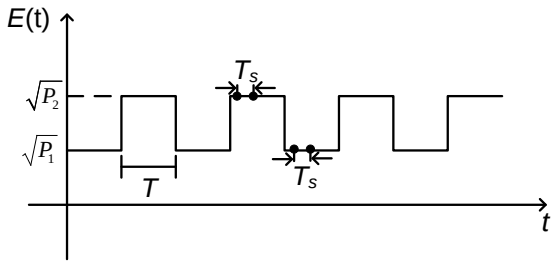

Fig. 5.3 A sequence of pilot symbols with alternating power levels P_1 and P_2 for the monitoring of laser linewidth, frequency offset, number of spans, fiber nonlinear parameters and OSNR of the link. The received signal is sampled at a rate of $1/T_s$ and the symbol rate $1/T$ is low enough such that the transmitted signal *E(t)* does not undergo any pulse shape distortion due to CD and/or PMD.

In absence of nonlinearity and when the symbol rate of the pilot symbols is low

enough so that the effects of CD and PMD are negligible, the instantaneous received signal power at time *t* can be expressed as

$$P(t) = \left| \sqrt{P_k} + \sum_{i=1}^{N} \left(n_{S_i}(t) + n_{D_i}(t) \right) \right|^2 \approx P_k + 2\sqrt{P_k}\ \mathrm{Re}\left\{ \sum_{i=1}^{N} \left(n_{S_i}(t) + n_{D_i}(t) \right) \right\} \quad \text{for } k = 1, 2 \text{ (5.2)}$$

where the approximation is valid for high OSNR. The variance of the received signal power P_k is then given by

$$\begin{aligned} \sigma^2_{power}(P_k) &= \mathbf{E}\left[P^2(t) \right] - \mathbf{E}\left[P(t) \right]^2 \\ &= \mathbf{E}\left[P_k^2 + 4P_k\sqrt{P_k}\ \mathrm{Re}\left\{ \sum_{i=1}^{N} \left(n_{S_i}(t) + n_{D_i}(t) \right) \right\} + 4P_k \left(\sum_{i=1}^{N} \mathrm{Re}\left\{ n_{S_i}(t) + n_{D_i}(t) \right\} \right)^2 \right] - P_k^2 \\ &= 2P_k N\left(\sigma_S^2 + \sigma_D^2 \right) \qquad \text{for } k = 1, 2. \text{ (5.3)} \end{aligned}$$

where $\sigma^2_{S(D)} = S_{S(D)}(f) B_f$ and B_f is the low-pass filter bandwidth at the receiver. It should be noted that Eq. (5.3) is still valid for systems with fiber nonlinearity.

The overall received phase $\phi(t)$ after propagating through *N* spans of fibers is given by

$$\phi(t) = \phi_{ASE}(t) + \phi_{NL}(t) + \phi_{Tx}(t) + \phi_{Rx}(t) + 2\pi\Delta f_{off} t + \theta \qquad (5.4)$$

which contains ASE-induced phase noise $\phi_{ASE}(t)$, nonlinear phase noise $\phi_{NL}(t)$ caused by fiber nonlinearity as well as transmitter and receiver laser phase noise $\phi_{Tx}(t)$ and $\phi_{Rx}(t)$. The frequency offset between the transmitter and receiver phase noise is denoted by Δf_{off} and θ is the relative phase of the transmitter (Tx) and

receiver (Rx) laser at $t = 0$. For high OSNR, the ASE-induced phase noise can be approximated as

$$\phi_{ASE}(t) \approx \frac{\mathrm{Im}\left\{\sum_{i=1}^{N}\left[n_{S_i}(t)+n_{D_i}(t)\right]\right\}}{\sqrt{P_k}} \qquad \text{for } k=1,2 \qquad (5.5)$$

with zero mean and variance

$$\sigma_{ASE}^2(P_k) = \frac{N}{2P_k}\left(\sigma_S^2+\sigma_D^2\right) \qquad \text{for } k=1,2. \quad (5.6)$$

Let γ_S and γ_D be the nonlinear coefficients of the SMF and DCF, and $L_{eff,S}$ and $L_{eff,D}$ be the effective lengths of SMF and DCF respectively. Defining $\Lambda_S = \gamma_S L_{eff,S}$ and $\Lambda_D = \gamma_D L_{eff,D}$, the overall nonlinear phase shift at the receiver is given by

$$\begin{aligned}
\phi_{NL}(t) &= \Lambda_S\left|\sqrt{P_k}\right|^2 + \Lambda_D\left|\sqrt{P_k}+n_{S_1}(t)\right|^2 \\
&\quad + \Lambda_S\left|\sqrt{P_k}+n_{S_1}(t)+n_{D_1}(t)\right|^2 + \Lambda_D\left|\sqrt{P_k}+n_{S_1}(t)+n_{D_1}(t)+n_{S_2}(t)\right|^2+\cdots \\
&\quad + \Lambda_S\left|\sqrt{P_k}+n_{S_1}(t)+\cdots n_{S_{N-1}}(t)+n_{D_1}(t)+\cdots+n_{D_{N-1}}(t)\right|^2 \\
&\quad + \Lambda_D\left|\sqrt{P_k}+n_{S_1}(t)+\cdots\cdots n_{S_N}(t)+n_{D_1}(t)+\cdots\cdots+n_{D_{N-1}}(t)\right|^2 \\
&= \sum_{i=1}^{N}\left(\Lambda_D\left|\sqrt{P_k}+\sum_{l=1}^{i}n_{S_l}(t)+\sum_{m=1}^{i-1}n_{D_m}(t)\right|^2+\Lambda_S\left|\sqrt{P_k}+\sum_{m=1}^{i-1}n_{S_m}(t)+\sum_{m=1}^{i-1}n_{D_m}(t)\right|^2\right) \\
&\approx \sum_{i=1}^{N}\Lambda_D\left(P_k+2\sqrt{P_k}\,\mathrm{Re}\left\{\sum_{l=1}^{i}n_{S_l}(t)+\sum_{m=1}^{i-1}n_{D_m}(t)\right\}\right) \\
&\quad + \sum_{i=1}^{N}\Lambda_S\left(P_k+2\sqrt{P_k}\,\mathrm{Re}\left\{\sum_{l=1}^{i-1}n_{S_l}(t)+\sum_{m=1}^{i-1}n_{D_m}(t)\right\}\right) \qquad \text{for } k=1,2. \quad (5.7)
\end{aligned}$$

where the approximation is valid for high OSNR. In this case, the mean and variance

of the nonlinear phase shift $\phi_{NL}(t)$ is given by

$$\overline{\phi_{NL}(P_k)} = P_k N\left(\Lambda_S + \Lambda_D\right) \qquad \text{for } k = 1,2 \quad (5.8)$$

and

$$\begin{aligned}
\sigma_{NL}^2(P_k) &= \mathrm{E}\left[\phi_{NL}^2(P_k)\right] - \mathrm{E}\left[\phi_{NL}(P_k)\right]^2 \\
&= 2P_k\left(\Lambda_S + \Lambda_D\right)^2 \sigma_D^2\left[(N-1)^2 + (N-2)^2 + \cdots + 1\right] \\
&\quad + 2P_k\sigma_S^2\left\{\left[\Lambda_S(N-1) + \Lambda_D N\right]^2 + \left[\Lambda_S(N-2) + \Lambda_D(N-1)\right]^2 + \cdots + \Lambda_D^2\right\} \\
&= 2P_k\left(\Lambda_S + \Lambda_D\right)^2 \sigma_D^2 \sum_{i=1}^{N-1} i^2 + 2P_k\sigma_S^2\left(\Lambda_S^2 \sum_{i=1}^{N-1} i^2 + \Lambda_D^2 \sum_{i=1}^{N} i^2\right) \\
&\quad + 4\Lambda_S\Lambda_D P_k\sigma_S^2 \sum_{i=0}^{N-1}(N-i)^2 - 4\Lambda_S\Lambda_D P_k\sigma_S^2 \sum_{i=0}^{N-1}(N-i) \qquad \text{for } k = 1,2.
\end{aligned}$$

As $\sum_{i=1}^{N} i^2 = \dfrac{N(N+1)(2N+1)}{6}$ and $\sum_{i=1}^{N} i = \dfrac{N(N+1)}{2}$,

$$\begin{aligned}
\sigma_{NL}^2(P_k) &= 2P_k\left(\Lambda_S + \Lambda_D\right)^2 \sigma_D^2 \frac{N(N-1)(2N-1)}{6} \\
&\quad + 2P_k\sigma_S^2\left[\Lambda_S^2 \frac{N(N-1)(2N-1)}{6} + \Lambda_D^2 \frac{N(N+1)(2N+1)}{6}\right] \\
&\quad + 4\Lambda_S\Lambda_D P_k\sigma_S^2\left[\frac{N(N+1)(2N+1)}{6} - \frac{N(N+1)}{2}\right] \\
&= 2P_k\left(\Lambda_S + \Lambda_D\right)^2\left(\sigma_S^2 + \sigma_D^2\right)\left(\frac{1}{3}N^3 - \frac{1}{2}N^2 + \frac{1}{6}N\right) \\
&\quad + 2P_k\sigma_S^2\left[\Lambda_D^2 N^2 + \Lambda_S\Lambda_D\left(N^2 - N\right)\right] \qquad \text{for } k = 1,2. \qquad (5.9)
\end{aligned}$$

Assuming Tx and Rx lasers with identical linewidth, the spectrum of the laser output $e^{j\phi_{Tx(Rx)}(t)}$ can be modeled as a Lorentzian lineshape with 3-dB linewidth Δf_{LW} in which

$$\mathbf{E}\left[e^{j(\phi_{Tx(Rx)}(t_1) - \phi_{Tx(Rx)}(t_2))}\right] = \exp(-\pi\Delta f_{LW}\left|t_1 - t_2\right|). \qquad (5.10)$$

Equivalently, the phase noise $\phi_{Tx(Rx)}(t)$ can be modeled as a Wiener process in which $\phi_{Tx(Rx)}(t_2)-\phi_{Tx(Rx)}(t_1)$ is Gaussian distributed with zero mean and variance

$$\sigma_{LW}^2 = 2\pi\Delta f_{LW}\left|t_1 - t_2\right|. \tag{5.11}$$

In the following section, we will derive equations to monitor the frequency offset, laser linewidth, number of spans *N*, OSNR as well as the nonlinear coefficients of the link from the statistics of the received power and phase difference. It should be noted that for the purpose of implementing advanced DSP algorithms like BP, it suffices to monitor the nonlinear parameter Λ_D as supposed to the fiber nonlinear coefficient γ_D.

5.1.2 Simultaneous and independent multi-parameter monitoring

The frequency offset between the Tx and Rx lasers and their linewidths can be obtained from the statistics of the phase difference between samples within a pilot symbol. Without loss of generality, let $\phi(t)$ and $\phi(t+w_1T_s)$ belong to the same pilot symbol with power $\sqrt{P_k}$ and $\phi(t)$ being the first sample of the symbol. The phase difference between these two samples is given by

$$\begin{aligned}\Delta\phi(w_1) &= \phi(t+w_1T_s)-\phi(t)\\ &= \left[\phi_{ASE}(t)+\phi_{NL}(t)+\phi_{Tx}(t)+\phi_{Rx}(t)\right]-\\ &\quad \left[\phi_{ASE}(t+w_1T_s)+\phi_{NL}(t+w_1T_s)+\phi_{Tx}(t+w_1T_s)+\phi_{Rx}(t+w_1T_s)\right]+2\pi\Delta f_{off}w_1T_s\end{aligned} \tag{5.12}$$

where $w_1 = 1, 2, \cdots \eta - 1$ denotes the number of sample delay and $\eta = T/T_s$ is the number of samples per symbol. As $\phi_{ASE}(t)$ and $\phi_{NL}(t)$ are uncorrelated with each

other [48] and $\phi_{ASE(NL)}(t)$ and $\phi_{ASE(NL)}(t+w_1T_s)$ are also uncorrelated if we choose the filter bandwidth $B_f = \frac{1}{2T_s}$, the mean and variance of $\Delta\phi(w_1)$ is given by

$$\overline{\Delta\phi(w_1)} = 2\pi\Delta f_{off} w_1 T_s \tag{5.13}$$

and

$$\sigma^2_{\Delta\phi,k}(w_1) = 2\sigma^2_{NL}(P_k) + 2\sigma^2_{ASE}(P_k) + 2\times 2\pi\Delta f_{LW} w_1 T_s \tag{5.14}$$

It is obvious from Eq. 5.14 that the linear and nonlinear phase noise variance $\sigma^2_{ASE}(P_k)$ and $\sigma^2_{NL}(P_k)$ do not depend on w_1. Therefore, for two values w_1 and w_2 such that $\phi(t), \phi(t+w_1T_s)$ and $\phi(t+w_2T_s)$ belong to the same pilot symbol, the difference between $\sigma^2_{\Delta\phi,k}(w_1)$ and $\sigma^2_{\Delta\phi,k}(w_2)$ can be expressed as

$$\sigma^2_{\Delta\phi,k}(w_1) - \sigma^2_{\Delta\phi,k}(w_2) = 2\times 2\pi\Delta f_{LW}(w_1 - w_2)T_s \tag{5.15}$$

With Eq. 5.13 and 5.15, the frequency offset and laser linewidth of the Tx and Rx lasers can be estimated by

$$\Delta f_{off} = \frac{\overline{\Delta\phi}(w_1)}{2\pi w_1 T_s} \tag{5.16}$$

and

$$\Delta f_{LW} = \frac{\sigma^2_{\Delta\phi,k}(w_2) - \sigma^2_{\Delta\phi,k}(w_1)}{4\pi(w_2 - w_1)T_s} \tag{5.17}$$

The statistics of the phase difference $\Delta\phi(w_1)$ also allow us to simultaneously and independently monitor the number of spans *N*, fiber nonlinear parameters as well as

OSNR of the link. In particular, if we choose $w_1 = \eta$, the two samples $\phi(t)$ and $\phi(t + w_1 T_s)$ will belong to different pilot symbols with different power levels. In this case, the mean and variance of the phase difference will be given by

$$\overline{\Delta\phi(\eta)} = (P_2 - P_1)N(\Lambda_S + \Lambda_D) + 2\pi\Delta f_{off} T \tag{5.18}$$

assuming the signal power at time *t* is $P(t) = P_1$.

As the parameters of SMF such as length, attenuation and nonlinear coefficients are usually known and relatively more consistent across a network compared to those of DCF in practice, we will assume the knowledge of σ_S^2 and Λ_S when monitoring the number of span *N*, fiber nonlinear coefficient and OSNR of the link. With Eq. 5.3, 5.6, 5.9, 5.14-5.18 and some algebraic manipulations, one obtain

$$\begin{aligned} 2(P_1+P_2)\sigma_S^2\left(\Lambda_S^2 - \Lambda_S\frac{\overline{\Delta\phi(\eta)}}{P_1-P_2}\right)N^3 + \Bigg[(P_1+P_2)\frac{\overline{\Delta\phi(\eta)}^2\sigma_{power}^2(P_1)}{3(P_1-P_2)^2P_1} + 2(P_1+P_2)\sigma_S^2\frac{\overline{\Delta\phi(\eta)}^2}{(P_1-P_2)^2} \\ -2(P_1+P_2)\Lambda_S\sigma_S^2\frac{\overline{\Delta\phi(\eta)}}{P_1-P} + \frac{\sigma_{power}^2(P_1)}{4P_1}\left(\frac{1}{P_1}+\frac{1}{P_2}\right) - \left(\sigma_{\Delta\phi,1}^2(w_1) + \sigma_{\Delta\phi,2}^2(w_2)\right)\Bigg]N^2 \\ -\frac{(P_1+P_2)\overline{\Delta\phi(\eta)}^2\sigma_{power}^2(P_1)}{2P_1(P_1-P_2)^2}N + \frac{(P_1+P_2)\overline{\Delta\phi(\eta)}^2\sigma_{power}^2(P_1)}{6P_1(P_1-P_2)^2} = 0 \end{aligned} \tag{5.19}$$

which is a cubic function of *N*. Subsequently, the fiber nonlinear parameter Λ_D and OSNR can be calculated by

$$\Lambda_D = \frac{\overline{\Delta\phi(\eta)} - 2\pi\Delta f_{off} T}{(P_1 - P_2)N} - \Lambda_S \tag{5.20}$$

and

$$\text{OSNR} = \frac{P_k}{N\left(\sigma_S^2 + \sigma_D^2\right)} = \frac{P_k}{\frac{\sigma_{power}^2}{2P_k}} = \frac{2P_k^2}{\sigma_{power}^2} \qquad \text{for } k = 1, 2. \qquad (5.21)$$

In summary, we can estimate frequency offset, laser linewidth, number of spans, fiber nonlinear parameter and OSNR of a transmission link by choosing arbitrary values of P_1, P_2, w_1 and w_2 ($P_1 \neq P_2$ and $w_1 \neq w_2$) and solving for Eq. 5.16, 5.17, 5.19, 5.20 and 5.21.

5.2 Simulation Results and Discussions

Simulations are conducted in Matlab environment to investigate the monitoring performance of Δf_{off} , Δf_{LW} ,N, Λ_D and OSNR. Pilot sequences with 10^6 symbols with NRZ pulse shape are transmitted at two arbitrarily chosen power levels of $P_1 = -3$ dBm and $P_2 = -2$ dBm. The symbol rate is chosen to be 50 MSym/s so that the effects of CD and PMD become negligible. The sampling rate is set to be 25 GHz and thus $\eta = 500$. Other channel parameters are listed in Table 1. To maximize the monitoring range of Δf_{off} for a given sampling rate, w_1 is chosen to be 1. In addition, we arbitrarily set $w_2 = 3$ for laser linewidth monitoring. Simulation results for frequency offset and laser linewidth monitoring for a 15-span system are shown in Fig. 5.4(a)Fig. 5.4(b) for full CD compensated and 10% CD under-compensated links. The means and standard deviations of the estimates are obtained from 10 independent trials. From the figures, the proposed technique enables a wide monitoring range from -10 GHz to 10GHz, more than sufficient for worst cases of ± 5 GHz reported in practical systems [31]. The corresponding maximum estimation

error is below 6 MHz. For laser linewidth monitoring, a wide dynamic range of 100 kHz to 10 MHz with corresponding maximum estimation error below 1% is achieved. Such monitoring performance is comparable to others reported in the literature [37] that only monitors laser linewidths. It is also noted that the monitoring performance does not depend on the dispersion map of the transmission link.

Table 5.1 Channel parameters used in simulations

Parameter	Value	Parameter	Value
α_S	0.25 dB/km	α_D	0.6 dB/km
L_S	80 km	L_D	16 km for full CD compensation 14.4 km for 10% CD under-compensation
D_S	17 ps/km · nm	D_D	-85 ps/km · nm
n_{sp}	2	ν	193.1 THz
γ_S	1.2 W^{-1}/km		

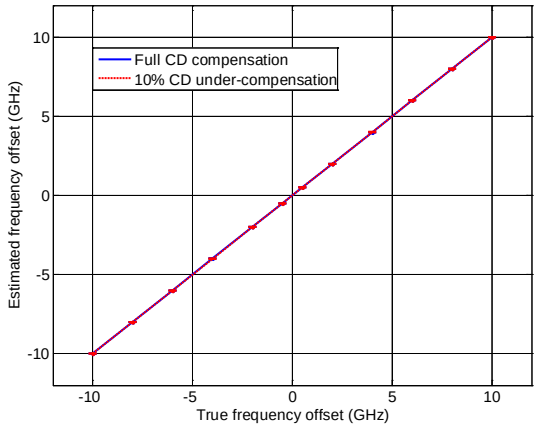

(a)

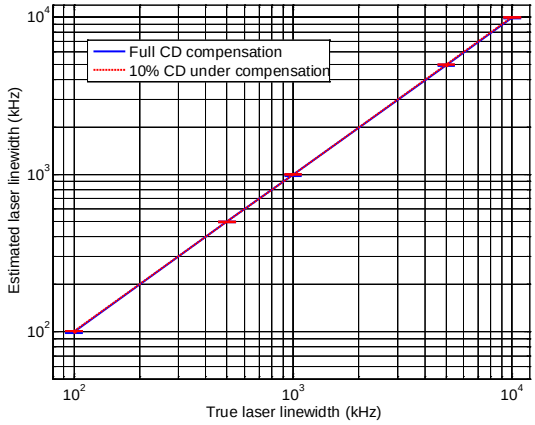

(b)

Fig. 5.4 (a) Estimated frequency offset vs. true frequency offset (b) Estimated laser linewidth vs. true laser linewidth for a 15-span system. Samples from 10^6 symbols are used for each estimate and the error bars indicate standard deviations of 10 independent estimates.

To ensure the monitoring accuracy of N, Λ_D and OSNR, the samples are further low-pass filtered with a bandwidth of 800 MHz and correspondingly down-sampled to eliminate the effect of CD on ASE noise. Fig. 5.5 shows the estimated N, OSNR and Λ_D vs. their true values for full CD compensated and 10% CD under-compensated links. The frequency offset and the laser linewidths are 200 MHz and 100 kHz respectively. As shown in Fig. 5.5(a), the mean of the estimated N generally agrees with their true values for $N \leq 22$. The slight inaccuracies for $N > 22$ may be caused by accumulated CD, frequency offset, laser linewidth, or a combination of them. Although the estimation errors gradually increase with N, the errors are limited to 1 span for a 25-span system. The accuracy of OSNR monitoring shown in Fig. 5.5(b) for both dispersion maps are within 0.1 dB and the dispersion map seems to have no obvious impact on OSNR monitoring. Fig. 5.5(c) shows the estimated Λ_D for different values of Λ_D for a system with N = 20. Although

estimation errors can be observed for both dispersion maps, the errors are limited to 0.4 dB and 0.6 dB (or equivalently 0.51 and 0.78 W^{-1}/km in γ_D) for full CD compensated and 10% CD under-compensated links respectively.

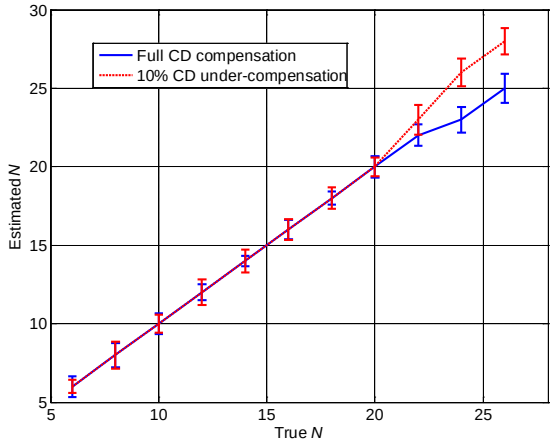

(a)

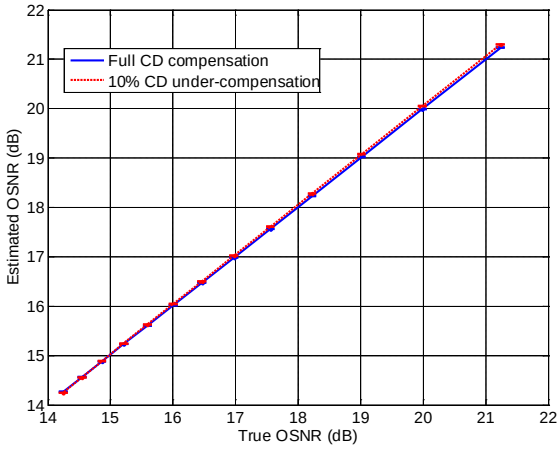

(b)

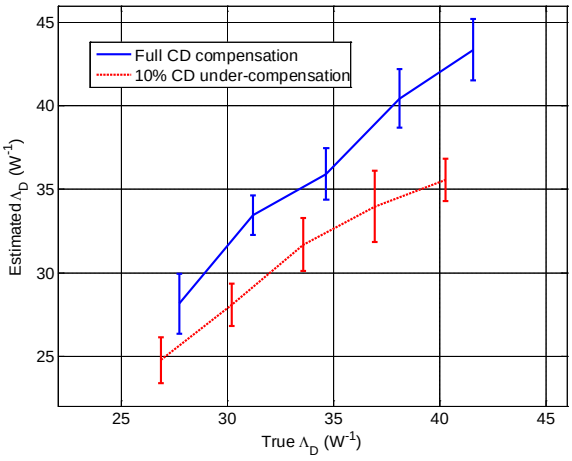

(c)

Fig. 5.5 (a) Estimated *N* vs. true *N*. (b) Estimated OSNR vs. true OSNR. (c) Estimated Λ_D vs. true Λ_D. Samples from 10^6 symbols are used for each estimate and the error bars indicate standard deviations of 10 independent estimates. The frequency offset and laser linewidth are 200 MHz and 100 kHz respectively.

5.3 Receiver-based fault localization using statistics of received pilot symbols

Data communications in optical networks can be interrupted by different types of faults along the link such as fiber cut, fiber bend and/or malfunctioning of inline optical amplifiers that result in sudden OSNR degradation or complete failure of the link. Locating the position of such faults is crucial to network operators for efficient channel restoration and maintaining high quality of service (QoS) in dynamic network environments. When there is an undesired drop in signal power, the extra gain required to amplify the signal back to pre-determined levels will produce additional ASE noise which result in OSNR degradations at the receiver [7]. To locate faults, tunable OTDR is proposed in [43] for the localization of fiber cut and serious degradation in OSNR. In [6], an optical transceiver is assigned to each predefined monitoring cycles to setup a dedicated supervisory channel. However,

introduction of additional optoelectronic components will increase the cost of installation and maintenance, especially in large scale networks. Meanwhile, Sichani *et al.* [4] demonstrated the use of limited-perimeter vector matching fault-localization protocol to achieve efficient fault localization in large scale networks by analyzing the alarm message issued by multiple devices. One disadvantage of this approach is that at least two distinct lightpaths with separate source-destination pairs are required [5].

If we regularly insert the pilot symbols studied in this paper between data transmission, it is actually possible to locate faults without the need of monitoring equipments at intermediate points of the link by studying the changes in the statistics of the received signal power and phase difference. In particular, from Eq. 5.3 and 5.9, if sudden OSNR degradations occur at the i^{th} span, the increase in the ASE noise power of the i^{th} amplifier $\Delta\sigma_i^2$ will induce the same change in the received power variance $\Delta\sigma_{power}^2(P_k)$ regardless of the value of i. However, the induced change in the variance of phase difference $\Delta\sigma_{\Delta\phi,k}^2(1)$ will actually depend on i. Intuitively, this is because ASE noise introduced earlier in the transmission link undergoes more fiber nonlinear effects and accumulates more nonlinear phase noise. Therefore, by monitoring the changes in $\Delta\sigma_{power}^2(P_k)$ and $\Delta\sigma_{\Delta\phi,k}^2(1)$ due to sudden OSNR degradations, one can determine the amount and location of the additional ASE noise introduced in the link which in turn serves as an indication of the location of the fault.

A calibration graph of the fault locations indexed according to the number of span starting from the transmitter vs. $\Delta\sigma_{\Delta\phi,k}^2(1)$ for different $\Delta\sigma_{power}^2(P_k)$ is given in Fig. 5.6

for a 20-span link. The other parameters of the pilot sequence and the channel used in the simulation are identical to those in Section 5.2. From the figure, for a given $\Delta\sigma^2_{power}(P_k)$, the change in variance of phase difference $\Delta\sigma^2_{\Delta\phi,k}(1)$ is distinct for different fault locations. In a network where fault locations are detected through other means, the proposed method may provide additional information about the status of the network and simplify network layer communication protocols and enhance efficiencies in network management.

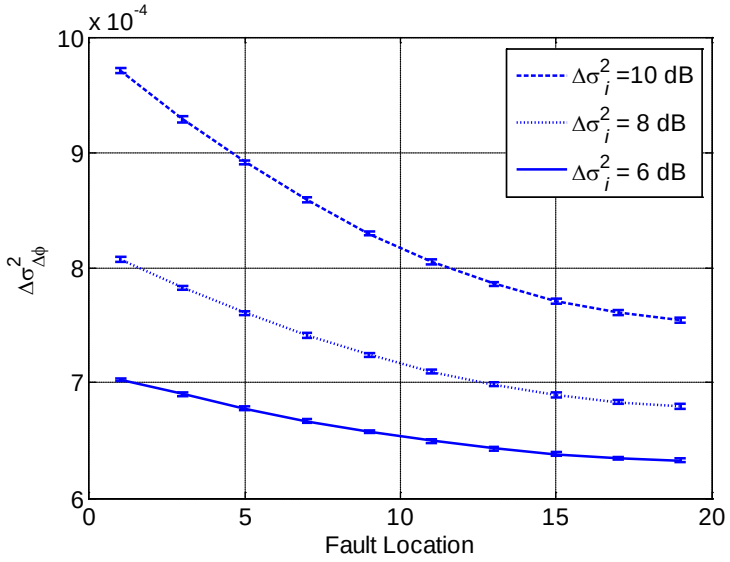

Fig. 5.6 Change in variance of phase difference $\Delta\sigma^2_{\Delta\phi}(1)$ vs. fault location with $\Delta\sigma^2_{power}(P_k)$ = 6, 8 and 10 dB for a 20-span link. Samples from 10^6 symbols are used for each estimate and the error bars indicate standard deviations of 10 independent estimates.

5.4 Summary

In this chapter, we present the first work on monitoring of nonlinear channel impairments. We proposed the use of pilot symbols prior to data transmission and study the statistics of the received power and phase difference to monitor laser frequency offset, laser linewidth, the number of spans, the fiber nonlinear

parameters as well as the OSNR of the link. For links with full CD compensation or 10% CD under-compensation per span, simulation results indicated that simultaneous and independent monitoring of multiple parameters can be achieved with good monitoring range and accuracies. In addition, examining the changes in the statistics of received power and phase difference enable us to locate faults along a given transmission link without the need for monitoring equipments at intermediate nodes of the link.

Chapter 6
SUMMARY AND FUTURE WORK

6.1 Summary of the work

Optical performance monitoring is essential to the operation of intelligent and flexible optical networks. Having access to the physical states of the channel, the network management system will be able to identify subtle changes in the physical channel which cannot be seen by conventional fault management system and take precautions to prevent sudden performance outage. Real-time information of channel impairments will enable the network to implement impairment-aware routing for better network performance. OPM is also a fundamental function to realize self-diagnose and self-reconfiguration in the next generation optical communication systems. Knowledge about the physical channel can facilitate adaptive transmission strategies and flexible network topologies that maximize network efficiencies.

OSNR is the most commonly monitored channel parameter, as it is a direct and fundamental measurement of signal quality in the channel. CD and PMD effects are also typical channel impairments monitored in high speed optical networks. As we are moving towards the optical coherent networks, monitoring of nonlinear impairments caused by fiber nonlinearity and other phase impairments such as laser phase noise and laser frequency offset is becoming more and more important.

Despite the need for OPM, several major challenges still need to be resolved before practical OPM techniques can be fully integrated in future networks. In

general, OPM techniques suffer from the trade-off between monitoring range and monitoring accuracy. It is also difficult to distinguish the effect of different channel impairments on the signal for independent monitoring of each type of impairment. The cost of monitoring equipment is another important parameter in OPM design.

In Chapter III, application of asynchronous amplitude histogram in OSNR monitoring for systems using higher order modulation formats such as 16-QAM and 64-QAM was studied. The number of identifiable AAH peaks varies with modulation formats and the shape of AAH changes with OSNR. To increase the sensitivity of the monitoring technique, the means and standard deviations of the last two peaks of the AAH are used to calculate a parameter for OSNR monitoring. Simulation results demonstrated a wide monitoring range of 12 to 40 dB for both NRZ/ RZ formats with monitoring sensitivities exceeding 1.75 dB for each dB change in OSNR. Since only the largest two peaks of the histogram are used to monitor OSNR, the proposed technique can be applied to any modulation formats with two or more power levels. Tolerance of the monitoring technique to CD and PMD is also studied.

As simultaneous and independent monitoring of multiple channel impairments with good monitoring and accuracy is not achievable using AAH alone, artificial neural network trained with asynchronous amplitude histograms was proposed in Chapter IV as a low-cost alternative for accurate simultaneous OSNR, CD and PMD monitoring. It has been shown that AAH presents distinct visual features when subject to different impairment combinations. As AAH itself is the empirical

distribution of received signal amplitudes, the value and relative occurrence of each AAH bin is directly used as the input to ANN. Simulation results obtained from both 40 Gbps RZ-DQPSK and NRZ-16-QAM systems demonstrate high monitoring accuracies with similar dynamic ranges compared to other known ANN based techniques. Since only received signal amplitudes are measured and no timing/clock recovery is required, this particular ANN-based technique is transparent to different modulation formats and bit rates.

In Chapter V, it is shown that future DSP-based coherent communication systems require detail and accurate knowledge of transmission link parameters for implementation of advanced impairment compensation algorithms such as digital back-propagation. Pilot symbols are proposed to be transmitted prior to data transmission and the statistics of the received power and phase difference of the pilot symbols can be used for monitoring of laser frequency offset, laser linewidth, the number of spans, the fiber nonlinear parameters as well as OSNR of the link. For links with full CD compensation or 10% CD under-compensation per span, simulation results indicated that simultaneous and independent monitoring of multiple parameters can be achieved with good monitoring range and accuracies. In addition, examining the changes in the statistics of received power and phase difference enables fault localization along a given transmission link without the need for monitoring equipments at intermediate nodes of the link.

6.2 Suggestion for future work

As discussed in previous sections, modern optical performance monitoring requires the monitoring techniques to be transparent to modulation formats and bit rate. It is also desired that the same monitoring technique can simultaneously monitor multiple channel impairments. The work presented in this thesis has improved existing approaches and proposed new techniques to satisfy these criteria. Monitoring of fiber nonlinearity is also studied for the first time in the thesis. However, there is still room for further improvement to meet the demand on OPM in future networks.

AAH-based OSNR monitoring techniques are known to be sensitive to other channel impairments. Exploring the combination of AAH with algorithms besides ANN may help eliminate such dependency and extend the monitoring range. The impact of CD, PMD and nonlinearity on AAH when OSNR varies could also be accounted in a comprehensive mathematical model. Analytical solutions to the derived equations could possibly enable independent OSNR monitoring.

It is demonstrated that ANN can easily achieve simultaneous monitoring of OSNR, CD and PMD given proper training sets. It will be worthy of exploring other input to ANN for larger monitoring range and higher monitoring accuracy such as RF spectrum. On the other hand, more in-depth study on ANN may also help investigate the feature of the input actually leads to the estimation of a particular impairment. Upon the success of this study, one may be able to distinguish and monitor multiple channel impairments with appropriate signal processing techniques.

Finally, further investigations on nonlinearity monitoring are vital for its implementation in future optical networks. The effect of CD on the means and variances of received signal power and phase should be included or better isolated in future analytical derivations so that the symbol rate of pilot tone does not need to be that low and the transmission period reserved for pilot symbols could be shortened. The impact of filter shape, polarization dependent loss (PDL), XPM in WDM system on the performance of the proposed monitoring technique will also be studied in future work.

REFERENCES:

[1] Z. Q. Pan, C. Y. Yu, and A. E. Willner, "Optical performance monitoring for the next generation optical communication networks," *Optical Fiber Technology,* vol. 16, pp. 20-45, Jan 2010.

[2] C. C. K. Chan, *Optical performance monitoring : advanced techniques for next-generation photonic networks*. Burlington, MA: Academic Press/Elsevier, 2010.

[3] E. Mannie, "Generalized multi-protocol label swtiching (GMPLS) Architecture," *IETF RFC 3945,* Oct. 2004.

[4] A. V. Sichani and H. T. Mouftah, "Limited-perimeter vector matching fault-localization protocol for transparent all-optical communication networks," *IET Communications,* vol. 1, pp. 472-478, Jun 2007.

[5] M. Khair, B. Kantarci, J. Zheng, and H. T. Mouftah, "Optimization for fault localization in all-optical Networks," *Journal of Lightwave Technology,* vol. 27, pp. 4832-4840, Sep 2009.

[6] S. S. Ahuja, S. Ramasubramanian, and M. Krunz, "Single-link failure detection in all-optical networks using monitoring cycles and paths," *IEEE/ACM Transactions on Networking,* vol. 17, pp. 1080-1093, Aug 2009.

[7] Y. G. Wen, V. W. S. Chan, and L. Z. Zheng, "Efficient fault-diagnosis algorithms for all-optical WDM networks with probabilistic link failures," *Journal of Lightwave Technology,* vol. 23, pp. 3358-3371, Oct 2005.

[8] M. N. Petersen, "Performance monitoring in the next generation of optical networks," *Proceedings of International Conference on Photonics in Switching, Heraklion, Crete,* pp. 120-122, Oct 2006.

[9] A. G. Green, P. P. Mitra, and L. G. L. Wegener, "Effect of chromatic dispersion on nonlinear phase noise," *Optics Letters,* vol. 28, pp. 2455-2457, Dec 2003.

[10] I. Shake and H. Takara, "Chromatic dispersion dependence of asynchronous amplitude histogram evaluation of NRZ signal," *Journal of Lightwave Technology,* vol. 21, pp. 2154-2161, Oct 2003.

[11] X. X. Wu, J. A. Jargon, R. A. Skoog, L. Paraschis, and A. E. Willner, "Applications of artificial neural networks in optical performance monitoring," *Journal of Lightwave Technology,* vol. 27, pp. 3580-3589, Aug 2009.

[12] Q. Yu, Z. Q. Pan, L. S. Yan, and A. E. Willner, "Chromatic dispersion monitoring technique using sideband optical filtering and clock phase-shift detection," *Journal of Lightwave Technology,* vol. 20, pp. 2267-2271, Dec 2002.

[13] J. P. Gordon and L. F. Mollenauer, "Phase noise in photonic communications-systems using linear-amplifiers," *Optics Letters,* vol. 15, pp. 1351-1353, Dec 1990.

[14] A. P. T. Lau and J. M. Kahn, "Signal design and detection in presence of nonlinear phase noise," *Journal of Lightwave Technology,* vol. 25, pp. 3008-3016, Oct 2007.

[15] E. Ip and J. M. Kahn, "Compensation of dispersion and nonlinear impairments using digital backpropagation," *Journal of Lightwave Technology,* vol. 26, pp. 3416-3425, Oct 2008.

[16] E. F. Mateo and G. F. Li, "Compensation of interchannel nonlinearities using enhanced coupled equations for digital backward propagation," *Applied Optics,* vol. 48, pp. F6-F10, Sep 2009.

[17] M. N. Petersen, Z. Pan, S. Lee, S. A. Havstad, and A. E. Willner, "Online chromatic dispersion monitoring and compensation using a single inband subcarrier tone," *IEEE Photonics Technology Letters,* vol. 14, pp. 570-572, Apr 2002.

[18] J. Zhao, A. P. T. Lau, K. K. Qureshi, Z. Li, C. Lu, and H. Y. Tam, "Chromatic dispersion monitoring for DPSK systems using RF power spectrum," *Journal of Lightwave Technology,* vol. 27, pp. 5704-5709, Dec 2009.

[19] I. Shake, W. Takara, S. Kawanishi, and Y. Yamabayashi, "Optical signal quality monitoring method based on optical sampling," *Electronics Letters,* vol. 34, pp. 2152-2154, Oct 1998.

[20] I. Shake, E. Otani, H. Takara, K. Uchiyama, Y. Yamabayashi, and T. Morioka, "Bit rate flexible quality monitoring of 10 to 160Gbit/s optical signals based on optical sampling technique," *Electronics Letters,* vol. 36, pp. 2087-2088, Dec 2000.

[21] I. Shake and H. Takara, "Averaged Q-factor method using amplitude histogram evaluation for transparent monitoring of optical signal-to-noise ratio degradation in optical transmission system," *Journal of Lightwave Technology,* vol. 20, pp. 1367-1373, Aug 2002.

[22] C. M. Weinert, C. Schmidt, and H. G. Weber, "Application of asynchronous amplitude histograms for performance monitoring of RZ signals," presented at the Optical Fiber Communication Conference and Exhibit (OFC), paper no. WDD41-1, 2001.

[23] B. Kozicki, O. Takuya, and T. Hidehiko, "Optical performance monitoring of phase-modulated signals using asynchronous amplitude histogram analysis," *Journal of Lightwave Technology,* vol. 26, pp. 1353-1361, Jun 2008.

[24] R. S. Luis, A. Teixeira, and P. Monteiro, "Optical signal-to-noise ratio estimation using reference asynchronous histograms," *Journal of Lightwave Technology,* vol. 27, pp. 731-743, Apr 2009.

[25] Z. H. Li and G. F. Li, "In-line performance monitoring for RZ-DPSK signals using asynchronous amplitude histogram evaluation," *IEEE Photonics Technology Letters,* vol. 18, pp. 472-474, Jan 2006.

[26] Z. H. Li and G. F. Li, "Chromatic dispersion and polarization-mode dispersion monitoring for RZ-DPSK signals based on asynchronous amplitude-histogram evaluation," *Journal of Lightwave Technology,* vol. 24, pp. 2859-2866, Jul 2006.

[27] J. A. Jargon, X. X. Wu, and A. E. Willner, "Optical performance monitoring using artificial neural networks trained with eye-diagram parameters," *IEEE Photonics Technology Letters,* vol. 21, pp. 54-56, Jan 2009.

[28] J. A. Jargon, X. X. Wu, H. Y. Choi, Y. C. Chung, and A. E. Willner, "Optical performance monitoring of QPSK data channels by use of neural networks trained with parameters derived from asynchronous constellation diagrams," *Optics Express,* vol. 18, pp. 4931-4938, Mar 2010.

[29] T. B. Anderson, A. Kowalczyk, K. Clarke, S. D. Dods, D. Hewitt, and J. C. Li, "Multi impairment monitoring for optical networks," *Journal of Lightwave Technology,* vol. 27, pp. 3729-3736, Aug 2009.

[30] Y. Han and G. F. Li, "Coherent optical communication using polarization multiple-input-multiple-output," *Optics Express,* vol. 13, pp. 7527-7534, Sep 2005.

[31] T. Tanimura, T. Hoshida, S. Oda, H. Nakashima, M. Yuki, T. Zhenning, L. Ling, and J. C. Rasmussen, "Digital clock recovery algorithm for optical coherent receivers operating independent of laser frequency offset," presented at the 34th European Conference on Optical Communication, (ECOC), Brussels, Belgium, paper no. Mo.3.D.2 2008.

[32] S. L. Zhang, L. Xu, J. J. Yu, M. F. Huang, P. Y. Kam, C. Y. Yu, and T. Wang, "Novel ultra wide-range frequency offset estimation for digital coherent optical receiver," presented at the Optical Fiber Communication/National Optic Fiber Engineers Conference, (OFC/NOFEC), San Diego, CA, paper no. OWV3, 2010.

[33] Y. Cao, S. Yu, J. Shen, W. Y. Gu, and Y. F. Ji, "Frequency estimation for optical coherent MPSK system without removing modulated data phase," *IEEE Photonics Technology Letters*, vol. 22, pp. 691-693, Apr 2010.

[34] A. P. T. Lau, T. S. R. Shen, W. Shieh, and K. P. Ho, "Equalization-enhanced phase noise for 100Gb/s transmission and beyond with coherent detection," *Optics Express*, vol. 18, pp. 17239-17251, Aug 2010.

[35] J. A. Constable and I. H. White, "Laser linewidth measurement using a mach-zehnder interferometer and an optical amplifier," *Electronics Letters*, vol. 30, pp. 140-142, Jan 20 1994.

[36] T. Okoshi, K. Kikuchi, and A. Nakayama, "Novel method for high-resolution measurement of laser output spectrum," *Electronics Letters*, vol. 16, pp. 630-631, 1980.

[37] T. Duthel, G. Clarici, C. R. S. Fludger, J. C. Geyer, C. Schulien, and S. Wiese, "Laser linewidth estimation by means of coherent detection," *IEEE Photonics Technology Letters*, vol. 21, pp. 1568-1570, Oct 2009.

[38] S. O. Rice, "Statistical properties of a sine-wave plus random noise," *Bell System Technical Journal*, vol. 27, pp. 109-157, 1948.

[39] K. P. Ho and J. M. Kahn, "Electronic compensation technique to mitigate nonlinear phase noise," *Journal of Lightwave Technology*, vol. 22, pp. 779-783, Mar 2004.

[40] A. P. T. Lau, S. Rabbani, and J. M. Kahn, "On the statistics of intrachannel four-wave mixing in phase-modulated optical communication systems," *Journal of Lightwave Technology*, vol. 26, pp. 2128-2135, July 2008.

[41] K. S. Kim, R. H. Stolen, W. A. Reed, and K. W. Quoi, "Measurement of the nonlinear index of silica-core and dispersion-shifted fibers," *Optics Letters*, vol. 19, pp. 257-259, Feb 1994.

[42] T. Kato, Y. Suetsugu, M. Takagi, E. Sasaoka, and M. Nishimura, "Measurement of the nonlinear refractive-index in optical-fiber by the cross-phase-modulation method with depolarized pump light," *Optics Letters*, vol. 20, pp. 988-990, May 1995.

[43] J. Park and I. W. Sandberg, "Universal approximation using radial-basis-function networks," *Neural Computation*, vol. 3, pp. 246-257, Jun 1991.

[44] A. L. Blum and P. Langley, "Selection of relevant features and examples in machine learning," *Artificial Intelligence*, vol. 97, pp. 245-271, Dec 1997.

[45] L. Prigent and J. P. Hamaide, "Measurement of fiber nonlinear Kerr coefficient by 4-wave-mixing," *IEEE Photonics Technology Letters*, vol. 5, pp. 1092-1095, Sep 1993.

[46] C. Xu and X. Liu, "Postnonlinearity compensation with data-driven phase modulators in phase-shift keying transmission," *Optics Letters*, vol. 27, pp. 1619-1621, Sep 2002.

[47] M. Mayrock and H. Haunstein, "Monitoring of linear and nonlinear signal distortion in coherent optical OFDM transmission," *Journal of Lightwave Technology*, vol. 27, pp. 3560-3566, Aug 2009.

[48] A. P. T. Lau and J. M. Kahn, "Design of inline amplifier gains and spacings to minimize the phase noise in optical transmission systems," *Journal of Lightwave Technology*, vol. 24, pp. 1334-1341, Mar 2006.